Tailoring Crystalline Phase and Surface of Lanthanide-Based Nanoparticles for MRI Applications

Nan Liu

A thesis submitted in partial fulfillment of the requirements for the

Master's degree in Chemistry

Department of Chemistry and Biomolecular Sciences

Faculty of Science

University of Ottawa

Abstract

Lanthanide-based nanoparticles (Ln^{3+}-based NPs) are promising candidates as magnetic resonance imaging (MRI) contrast agents. The present thesis aims to investigate the effect of the crystalline phase of Ln^{3+}-based NPs on their MRI contrast performance. Understanding the phase-dependent MRI contrast behaviour of Ln^{3+}-based NPs will provide insights into the development of brighter MRI contrast agents for future *in vivo* biomedical applications. A set of $NaGdF_4$ NPs (6-8 nm) in cubic and hexagonal phases in the same size range was synthesized by employing a microwave-assisted approach, allowing the influence of host crystallinity on MRI T_1 relaxivity to be investigated (chapter 4). The results showed that cubic $NaGdF_4$ NPs exhibited superior performance as MRI T_1 contrast agents than their hexagonal analogues, irrespective of the chosen surface modification, *e.g.* small citrate groups or longer chain poly(acrylic acid). $NaDyF_4$ NPs (3 nm) were synthesized in both phases to assess whether phase-dependent MRI contrast behaviour consistently exists in other Ln^{3+}-base NPs of the $NaLnF_4$ family (chapter 5). Again, it was demonstrated that cubic $NaDyF_4$ NPs had a better contrast performance as T_2 contrast agents than the hexagonal NPs. Alternatively, cubic $NaEuF_4$ NPs, exhibiting additional optical properties (*e.g.* red emission under UV excitation), were prepared as potential candidates for the preparation of chemical exchange saturation transfer (CEST) contrast agents (chapter 5). Chapter 6 introduces preliminary dispersion stability studies of cubic $NaGdF_4$ NPs dispersed in different buffer solutions, the obtained hydrodynamic diameters indicated that $NaGdF_4$ NPs possessed better dispersity in saline than that in PBS solution.

Acknowledgments

First and foremost, I would like to express my most sincere gratitude to my supervisor, Prof. Eva Hemmer, for offering me the opportunity to work in her research group. I am very grateful for her guidance, support and encouragement during my master's study. I would also like to thank her for introducing me to the very interesting world of lanthanide-based materials.

I express my appreciation to all collaborators for their grateful supports and inspiring discussions to my work presented in this thesis. I would like to thank Prof. Adam Shuhendler for sharing the MRI instrument to us and Dr. Greg Cron for performing MRI measurements with me. I thank Prof. Nicolas Bordenave for providing the NMR relaxometry. I also thank all the technical staffs in the Department of Chemistry and Biomolecular Sciences.

I would also like to thank all the members, both former and present, of the Hemmer group, for providing a space where we could learn from each other, support each and celebrate each other's achievements. In particular, I thank Dr. Riccardo Marin, Dr. Emille Martinazzo Rodrigues and Nikita Panov for TEM measurements; Illias Halimi for demonstrating the microscope operations; Dr. Isabel Gessner for her help in performing a successful surface modification procedure.

Finally, I would like to thank my parents and sisters for their support and endless love. I also want to thank my dear friends Xiafei Yu and Wenbo Wu for their company and encouragements.

Table of Contents

List of Tables

List of Figures

List of Abbreviations

CT	computer tomography
CEST	chemical exchange saturation transfer
DLS	dynamic light scattering
diaCEST	diamagnetic CEST agent
FTIR	Fourier transform infrared spectroscopy
FBS	fetal bovine serum
FDA	food and drug administration
Gd-DTPA	gadolinium-diethylene-etriaminepentacetate
Gd-DOTA	gadolinium-1,4,7,10-tetraazacyclododecane-1,4,7,10-tetraacetic acid
Gd-TFA	gadolinium trifluoroacetate
IS	inner sphere
ICP-OES	inductively coupled plasma optical emission spectroscopy
Ln	lanthanide
Ln^{3+}	trivalent lanthanide ions
Ln^{2+}	bivalent lanthanide ions
Ln^{4+}	tetravalent lanthanide ions
Ln-TFA	lanthanide trifluoroacetate
MRI	magnetic resonance imaging
NMR	nuclear magnetic resonance
NP	nanoparticle
OS	outer sphere
PET	positron emission tomography
PBS	phosphate-buffered saline solution
paraCEST	paramagnetic CEST agent
PEG	polyethylene glycol
PAA	poly(acrylic acid)
RF	radio frequency
S/V	surface-to-volume
SPIONs	super paramagnetic iron oxide nanoparticles

TFA	trifluoroacetic acid
TEM	transmission electron microscopy
TGA	thermogravimetric analyses
XRD	X-ray diffraction

Statement of Contribution

Some analytical techniques required in this thesis were performed by other technicians and colleagues. Namely, TEM images were obtained by Dr. Riccardo Marin, Dr. Emille Martinazzo Rodrigues and Nikita Panov. ICP-OES measurements were performed by Dr. Anabel Lanterna (University of Ottawa). TGA measurements were performed by Dr. Gwenael Chamoulaud (NanoQAM research center, University of Quebec, Montreal). MRI measurements were performed by Dr. Greg Cron and I. The other measurements including FTIR, DLS and Zeta potential were performed by myself. Part of this thesis was published in Nanoscale: N. Liu, R. Marin, Y. Mazouzi, G. O. Cron, A. Shuhendler, and E. Hemmer, Nanoscale, 2019, 11, 6794-6801. The manuscript written was under the guidance of Dr. Riccardo Marin and Prof. Eva Hemmer.

Chapter 1. Introduction

1.1 The Lanthanides

Lanthanides refer to the 15 elements located at the sixth period and IIIB group of the periodic table, atomic numbers ranging from element 57 (lanthanum) to 71 (lutetium) (Table 1.1).

Table 1.1. Electron configurations of the lanthanides and their common ions.

	Atom	**Ln^{3+}**	**Ln^{4+}**	**Ln^{2+}**
La	$[Xe]4f^0\,5d^1\,6s^2$	$[Xe]\,4f^0$		
Ce	$[Xe]\,4f^1\,5d^1\,6s^2$	$[Xe]\,4f^1$		
Pr	$[Xe]\,4f^3\,6s^2$	$[Xe]\,4f^2$	$[Xe]\,4f^1$	
Nd	$[Xe]\,4f^4\,6s^2$	$[Xe]\,4f^3$	$[Xe]\,4f^2$	$[Xe]\,4f^4$
Pm	$[Xe]\,4f^5\,6s^2$	$[Xe]\,4f^4$		
Sm	$[Xe]\,4f^6\,6s^2$	$[Xe]\,4f^5$		$[Xe]\,4f^6$
Eu	$[Xe]\,4f^7\,6s^2$	$[Xe]\,4f^6$		$[Xe]\,4f^7$
Gd	$[Xe]\,4f^7\,5d^1\,6s^2$	$[Xe]\,4f^7$		
Tb	$[Xe]\,4f^9\,6s^2$	$[Xe]\,4f^8$	$[Xe]\,4f^7$	
Dy	$[Xe]\,4f^{10}\,6s^2$	$[Xe]\,4f^9$	$[Xe]\,4f^8$	$[Xe]\,4f^{10}$
Ho	$[Xe]\,4f^{11}\,6s^2$	$[Xe]\,4f^{10}$		
Er	$[Xe]\,4f^{12}\,6s^2$	$[Xe]\,4f^{11}$		
Tm	$[Xe]\,4f^{13}\,6s^2$	$[Xe]\,4f^{12}$		$[Xe]\,4f^{13}$
Yb	$[Xe]\,4f^{14}\,6s^2$	$[Xe]\,4f^{13}$		$[Xe]\,4f^{14}$
Lu	$[Xe]\,4f^{14}\,5d^1\,6s^2$	$[Xe]\,4f^{14}$		

Studies on lanthanide (Ln) elements date back to the 18th century.[1] With the development of lanthanide chemistry for more than two centuries, these elements have found a wealth of applications in photonics, chemical industry, agriculture, and biomedicine.[2-4] In general, all the Ln elements have similar electronic configuration of $[Xe]4f^n\ 5d^{0-1}\ 6s^2$ (n = 0−14) (Table 1.1).[5] These elements are different from the main group elements because of their electrons in the f orbital. After Lanthanum, electrons start to fill the 4f sub-shell before the 5d sub-shell, because the energy of the 4f sub-shell falls below that of the 5d sub-shell. Generally, trivalent lanthanide ions (Ln^{3+}) are the most common and stable oxidation state of lanthanides, while some of the lanthanides may exist in their +2 (Ln^{2+}) and +4 (Ln^{4+}) oxidation states as their f orbitals are empty, half or fully occupied.

1.1.1 The Lanthanide Ions' Magnetic Properties

Ln^{3+} ions have unique magnetic and optical properties because of their 4f electrons, which are located inside the complete $5s^2$ and $5p^6$ shells, resulting in shielding of the 4f electrons from the local microenvironment.[6] With the exception of La^{3+} and Lu^{3+}, all Ln^{3+} ions contain unpaired electrons in their 4f orbitals and are paramagnetic.[7, 8] The magnetic moments and electronic relaxation times of Ln^{3+} ions are determined by their 4f electron configurations, which are different along the series. As shown in Table 1.2, the symmetric electron ground state of the Gd^{3+} ion results in weak spin−orbit coupling and consequently in long electronic relaxation times. Hence, Gd^{3+} ions can be used in magnetic resonance imaging (MRI) as T_1 contrast agents to shorten the relaxation time of protons.[9] On the contrary, the asymmetric electron ground states of Dy^{3+} and Ho^{3+} ions endow them with short electronic relaxation times but larger magnetic moments, which renders them suitable as MRI T_2 contrast agents.[8, 10, 11] An introduction to MRI technology will be given below (section 1.2).

Table 1.2. Magnetic moments of Ln^{3+} ions at room temperature.

Ln^{3+}	f^n	Ground term	Predicted μ_{eff} (μ_B)
Ce^{3+}	f^1	$^2F_{5/2}$	2.54
Pr^{3+}	f^2	$^3H_4$	3.58
Nd^{3+}	f^3	$^4I_{9/2}$	3.68
Pm^{3+}	f^4	$^5I_4$	2.83
Sm^{3+}	f^5	$^6H_{5/2}$	0.85
Eu^{3+}	f^6	$^7F_0$	0
Gd^{3+}	f^7	$^8S_{7/2}$	7.94
Tb^{3+}	f^8	$^7F_6$	9.72
Dy^{3+}	f^9	$^6H_{15/2}$	10.63
Ho^{3+}	f^{10}	$^5I_8$	10.62
Er^{3+}	f^{11}	$^4I_{15/2}$	9.59
Tm^{3+}	f^{12}	$^3H_6$	7.57
Yb^{3+}	f^{13}	$^2F_{7/2}$	4.53

1.1.2 The Lanthanide Ions' Optical Properties

Ln ions also have attractive optical property originating from intra-4f or 4f–5d transitions.[12] In fact, transitions between states of the same parity (such as f-f transitions) are forbidden by the Laporte selection rule, which is strict for Ln^{3+} ions in the gas phase but relaxed for ions embedded in a medium, where vibronic coupling and mixing of configurations can 'force' the electric dipole transitions to occur.[13] Consequently, Ln^{3+} ions doped into a suitable host exhibit narrow optical absorption and emission bands, high emission efficiency, and long excited state lifetimes.[14] The different electronic configurations of each Ln^{3+} ion result in different emission wavelengths, allowing multicolor applications.[15]

1.2 Magnetic Resonance Imaging (MRI)

MRI is currently one of the most powerful imaging technologies not only in clinical diagnosis but also in biological research.[16] It can provide the anatomical structure of soft tissues with cellular and even sub-cellular spatial resolutions in the micrometer realm,[17-19] and hence is now widely employed for the diagnosis of major diseases such as tumors, cardiovascular and cerebrovascular diseases.[19] MRI, as a non-invasive technique, has the potential to be less harmful compared to other imaging modalities that acquire similar images, such as computer tomography (CT) using X-rays and positron emission tomography (PET) using radioactive materials.[20]

In principle, MRI is achieved by detecting the relaxation signals of water proton spins in a strong magnetic field.[21] When the protons are exposed to an external magnetic field, the magnetic moments align either parallel or antiparallel to the magnetic field, producing a net magnetization along the longitudinal z axis (M_0) (Figure 1.1). After irradiating with a specific radio frequency (RF) pulse, the protons will be excited and the M_0 is flipped away from its original axis, inducing a magnetization on the perpendicular plane (M_{xy}). After the RF pulse disappears, the protons are not able to maintain their excited state and will return to the initial state, which is called relaxation.[22, 23] There are two independent relaxation processes: longitudinal (T_1) relaxation and transverse (T_2) relaxation. The former refers to the recovering of M_0 to the initial state ($M_{z(t)}$), which is also known as spin−lattice relaxation. The latter refers to the disappearing of M_{xy}, which is also known as spin−spin relaxation.

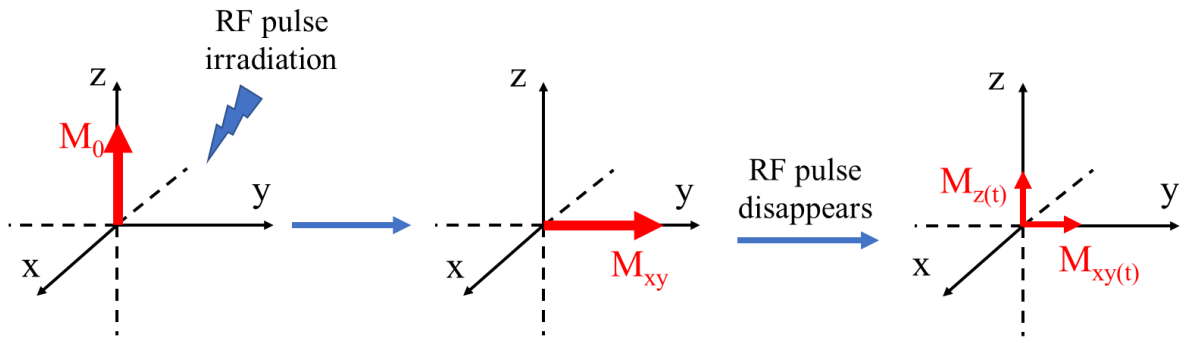

Figure 1.1. Principle of magnetic resonance imaging (MRI). A net magnetization (M_0) is produced in an external magnetic field. Irradiation of radio frequency (RF) makes M_0 flip away from the z axis to the xy plane (M_{xy}). After the RF pulse disappears, the protons relax to their initial state, in which M_0 increases and M_{xy} decreases. Redrawn from reference 20.

In the relaxation process, T_1 relaxation time is defined as the time required for $M_{z(t)}$ to recover to its equilibrium. T_1 relaxation is modeled as exponential growth curve with the time constant T_1 (equation 1.1):[24]

$$M_{z(t)} = M_0 \times (1 - e^{-t/T_1}) \tag{1.1}$$

Hence, T_1 can be viewed as the time (t) required for $M_{z(t)}$ to reach (1 − 1/e) or about 63% of its maximum value (M_0). The T_2 relaxation time is characteristic of the disappearance of M_{xy} (equation 1.2). Thus, T_2 is the time required for M_{xy} to drop to approximately 37% (1/e) of its initial value.[22]

$$M_{xy} = M_0 \times e^{-t/T_2} \tag{1.2}$$

The image contrast in MRI actually comes from the differences in the signal intensity of each pixel or voxel. In general, the signal intensity is determined by the local proton density, relaxation times (T_1 and T_2) of the protons as well as the pulse sequences.[25] The relaxation times of protons are dependent on their forms (*e.g.*, mobile or bound), which are quite different for various biological tissues, bringing intrinsic contrast.[26]

1.3 MRI Contrast Agents

An MRI contrast agent is any substance that can shorten the relaxation time of protons and enhance the MRI signals.[20, 27] The ability of a contrast agent to change the relaxation time is represented by its longitudinal relaxivity (r_1) and transverse relaxivity (r_2). Contrast agents with high relaxivities can provide better image contrast at a lower dose.[24, 28] Today, almost 50% of MR images use some form of contrast agents in clinic applications, and there have been a dozen US Food and Drug Administration (FDA) approved contrast agents.[29] In general, MRI contrast agents can be classified into two types: T_1 contrast agents (positive) and T_2 contrast agents (negative). T_1 contrast agents shorten spin–lattice relaxation time and typically enhance signal intensity, resulting in a brighter image; T_2 contrast agents shorten spin–spin relaxation time, causing a decrease in signal intensity and therefore leading to a darker image.[30-32] Both effects are described in more detail in the following paragraphs.

1.3.1 T_1 Contrast Agents

The Gd^{3+} ion has the highest number of unpaired electrons in its 4f electronic configuration and nearly no net orbital momentum, resulting in a negligible spin-orbit coupling. As a result, Gd^{3+} ions have a relatively long electronic relaxation time and have been widely used in MRI as T_1 contrast agents to enhance MRI signals.[33] However, Gd^{3+} ions cannot be used as free ions, due to toxicity concerns.[34] In order to overcome this hurdle, Gd^{3+}-chelates have been developed since the 1980s, and the first two commercial Gd^{3+}-chelates approved by FDA were gadolinium-diethylene-etriaminepentacetate (Gd-DTPA) and gadolinium-1,4,7,10-tetraazacyclododecane-1,4,7,10-tetraacetic acid (Gd-DOTA) (Figure 1.2).[34] The presence of Gd^{3+}-chelates in a particular location of a living tissue will result in a brighter signal (positive enhancement) in this region of the image (Figure 1.3).[24] Moreover, Gd^{3+}-chelates have an

immediate contrast effect, which means that diagnostic images appear within minutes after the administration of the Gd^{3+}-chelates to the patients. This makes Gd^{3+}-chelates suitable for fast imaging.[31] However, despite their frequent real-life application, there are still ongoing limitations for Gd^{3+}-chelates that are currently addressed by researchers. For instance, because of their low molecular weight, Gd^{3+}-chelates lack specificity and show limitations for long-term tracking.[16] In addition, there is also the possible occurrence of nephrogenic systemic fibrosis associated with exposure of these contrast agents to patients suffering from poor kidney function.[35-38]

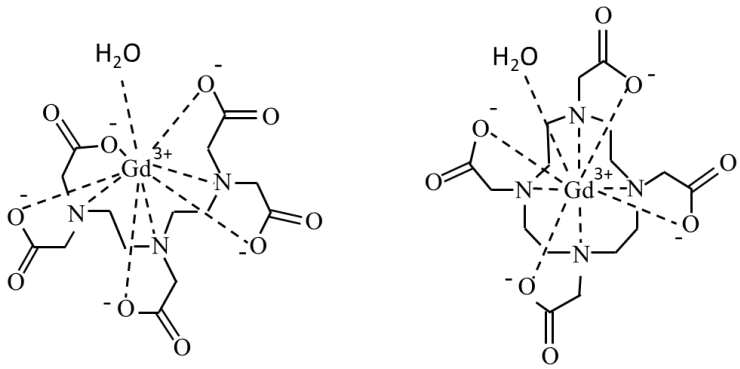

$[Gd(DTPA)(H_2O)]^{2-}$ $[Gd(DOTA)(H_2O)]^{-}$

Figure 1.2. Chemical structures of Gd-DTPA and Gd-DOTA.

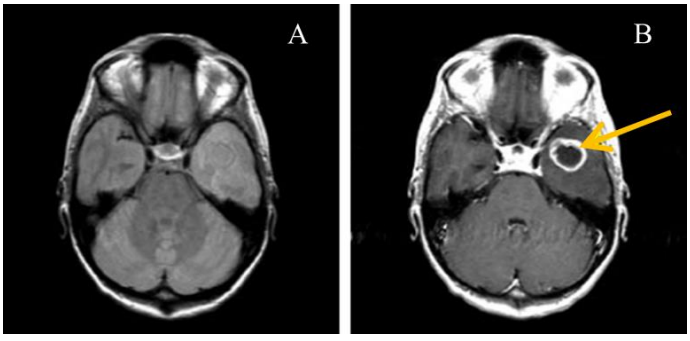

Figure 1.3. Images of a human brain with a tumor without (A) and with the use of a Gd^{3+}-chelate contrast agent (B) displaying the tumor (marked by the yellow arrow). Reproduced with permission from reference 24, Copyright © 2013 by John Wiley & Sons, Inc.

1.3.2 Gd^{3+}-based Nanoparticles as T_1 Contrast Agents

In order to address some of the limitations of Gd-chelates, Gd^{3+}-based nanoparticles (NPs), including gadolinium oxide (Gd_2O_3), sodium gadolinium fluoride ($NaGdF_4$), gadolinium oxysalts (*e.g.*, $GdPO_4$), and gadolinium hydroxide ($Gd(OH)_3$), have been extensively explored as alternative T_1 contrast agents.[22, 39, 40] These NPs have longer blood circulation time and a large density of Gd^{3+} ions on their surface when compared to Gd^{3+}-complexes, which dramatically increases the concentration of the contrast-providing species in the region of interest.[16, 41] Moreover, embedding Gd^{3+} ions into a matrix, such as inorganic nanoparticles, where they are firmly held, can reduce their leakage from the probe, lowering levels of free Gd^{3+} ions and hence contributing to lower toxicity.[42] In addition, these NPs can also be engineered with surface chemistries (*e.g.* anchoring functional groups) opening the path to multifunctional diagnostic and therapeutic agents.[43] Intensive research has been undertaken in order to describe and advance their performance as T_1-weighted contrast agents.[40, 41, 44-46] Factors influencing T_1 relaxivity are described in more detail in the following.

1.3.2.1 Effect of Size on T_1 Relaxivity

The relationship between NP size and T_1 relaxivity has been widely investigated. For instance, van Veggel *et al.* synthesized $NaGdF_4$ NPs with four different sizes (2 to 8 nm), and found that the r_1 value increased when the particle size decreased.[41] Talham *et al.* obtained the same trend with $Eu_{0.2}Gd_{0.8}PO_4 \cdot H_2O$ NPs.[47] For NPs with comparable surface chemistry and similar shapes, the surface-to-volume (S/V) ratio is strongly dependent on particle size, smaller sizes bringing higher S/V ratios. A higher S/V ratio will allow more surface Gd^{3+} ions to interact with water molecules and thus, result a larger r_1 value.[41, 46, 48] However, Gao *et al.* prepared $NaGdF_4$ NPs in three sizes (5, 15 and 20 nm) and found that both 5 nm and 20 nm-sized NPs

exhibited higher r_1 values than the 15 nm-sized NPs.[49] This was because there were two parameters affecting the r_1 value, S/V ratio and rotational correlation time (τ_R). τ_R indicates the tumbling rate of the NPs, and the slow tumbling rate (large τ_R) is in favor of higher r_1.[50] With the increasing NP size, the S/V ratio decreases but τ_R value increases. Hence, for 20 nm-sized NPs, the contribution of τ_R is dominated to obtain a higher r_1 value.[49] And in case of 5 nm-sized NPs, the S/V ratio is dominated. Combining the negative correlation between S/V and τ_R, a nonmonotonic behavior accompanied by size change is the result (Figure 1.4).[51]

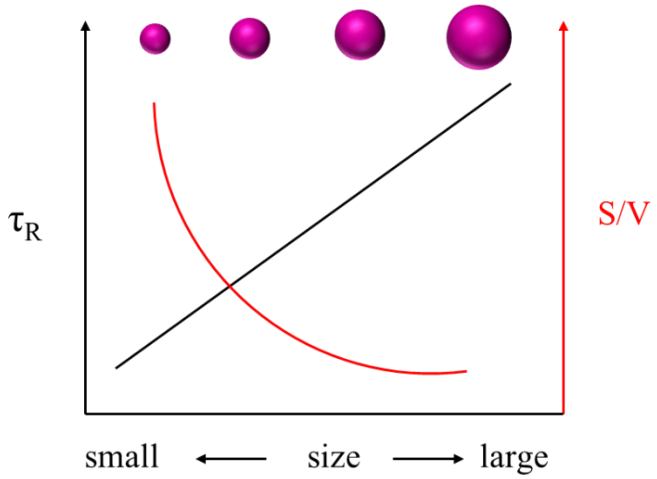

Figure 1.4. Scheme of size dependence of two parameters (τ_R and S/V) for spherical particles. When size increases, τ_R increases and S/V decreases, which is counteracting for relaxation enhancement. Reproduced with permission from reference 51, copyright © 2015, American Chemical Society.

1.3.2.2 Effect of Nanoparticles Agglomeration on T_1 Relaxivity

The effect of particle agglomeration on T_1 relaxivity has also been discussed in the literature. For example, Fortin *et al.* reported that the r_1 values of Gd_2O_3 NPs decreased when the particles aggregated.[52] This can be related to one of key aspects for achieving high r_1 values, which is the proximity of surface Gd^{3+} ions to the water protons. Therefore, the presence of a large number of surface Gd^{3+} ions would yield high r_1 values. However, upon NP aggregation, the number of surface Gd^{3+} ions would be decreased (Figure 1.5). Moreover, inside the

aggregates, there were probably fewer water molecules in close contact with Gd^{3+} ions compared to the situation prevailing in the outer boundaries of the nanoaggregates, which explained the gradual decline of r_1 values upon aggregation.

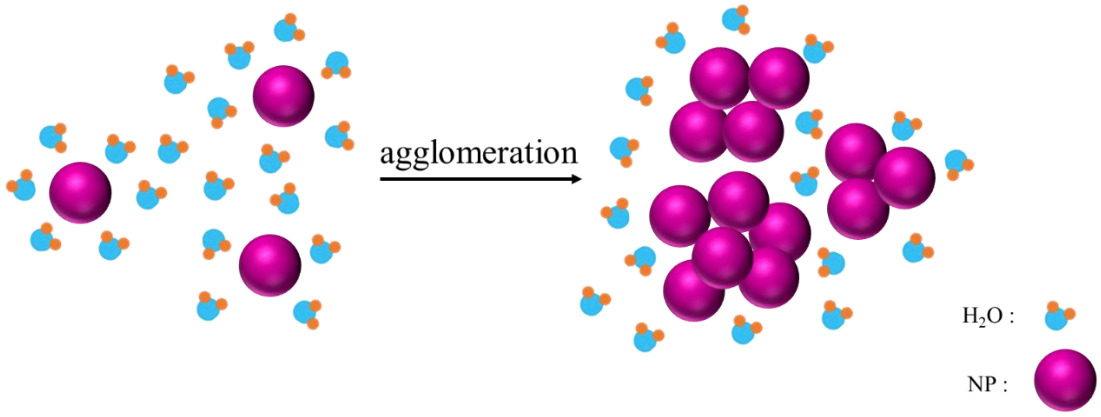

Figure 1.5. The effect of particles agglomeration on r_1 value. Particles agglomeration leads to fewer water molecules interacting with surface Gd^{3+} ions, resulting in smaller r_1 values.

1.3.2.3 Effect of Surface Modification on T_1 Relaxivity

In order to render the synthesised NPs (oleate-capped – *vide infra*) water dispersible for MRI applications, surface modifications have been performed for oleate-capped NPs.[53] The surface ligands not only decide the water-dispersibility and biocompatibility, but also influence the interaction between water molecules and surface Gd^{3+} ions.[54] In principle, the more interaction between water protons and surface Gd^{3+} ions, the larger T_1 relaxivity will be obtained. The effect of surface modification on T_1 relaxivity is summarized in Figure 1.6. It has been shown that ligand-free Gd_2O_3 NPs, the surface of which was not blocked by any chemical, had a higher r_1 value than the corresponding ligand-coated NPs.[55] It was believed that water protons get fairly close to the surface Gd^{3+} of the ligand-free Gd_2O_3 NPs as compared to ligand-coated ones, ultimately resulting in the increase of the r_1 value. Yet, for such an effect to happen, ligand-free NPs must be stable in dispersion without any agglomeration in the aqueous

medium. If the ligand-free NPs were aggerated (as often the case), the r_1 value would be smaller than that of the ligand-coated NPs due to fewer water molecules interacting with surface Gd^{3+} ions (as discussed above).[56]

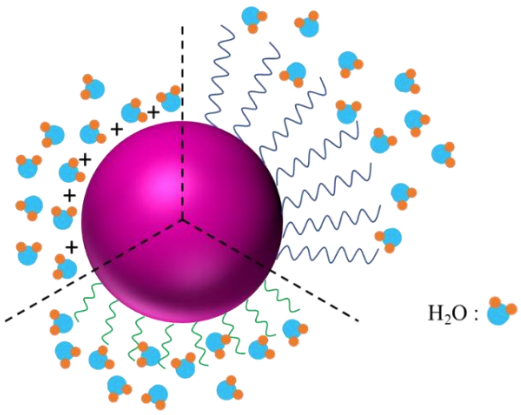

Figure 1.6. The effect of surface modification on T_1 relaxivity with ligand-free, short-ligand coating and long-ligand coating Gd^{3+}-based NPs, respectively.

Also, the ligand-size dependence of water proton relaxivities has been investigated for $NaGdF_4$ NPs with different types of ligands grafted to their surface. van Veggel *et al.* reported that the r_1 value of NPs coated with shorter ligands was larger than that obtained for coating with longer ligands.[57] This phenomenon was attributed to ligand-size effect on water accessibility to surface Gd^{3+} ions, that is, smaller ligands will allow more water molecules to access the surface Gd^{3+} ions.[58] In fact, the ligand-size also influences τ_R, and a longer ligand chain will slow the rotation of the NPs. In summary, a carefully designed surface modification of NPs is crucial for nanoparticulate T_1 contrast agents.

1.3.3 T_2 Contrast Agents

The typical T_2 contrast agents used for clinical applications are superparamagnetic iron oxide nanoparticles (SPIONs). These particles behave like small movable magnets, creating a strong

magnetic field inhomogeneity in their environment and considerably reducing the T_2 relaxation time of water protons in their vicinity (Figure 1.7).[59] SPIONs have low toxicity, good biocompatibility and biodegradability, as well as high sensitivity for low field imaging.[60] The r_2 relaxivity enhancement is mainly proportional to the saturation magnetization value and the surface area of the SPIONs. Hence, in order to achieve high performance, many attempts have been made to improve the magnetic moment by controlling NP size, composition and morphology. [25, 61, 62]

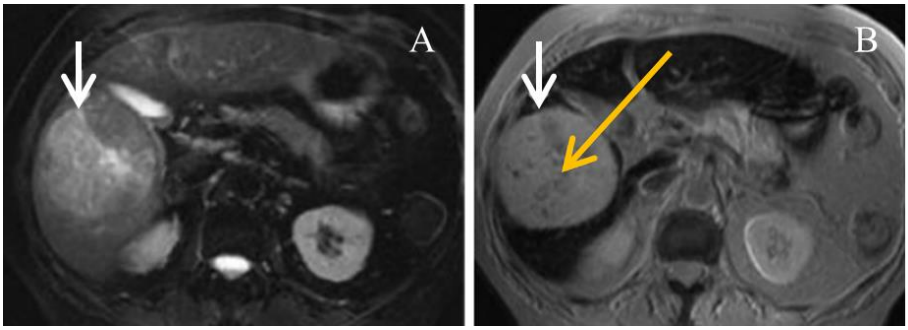

Figure 1.7. Images of a human liver without (A) and with (B) superparamagnetic iron oxide NPs, displaying normal liver tissue with dark spots (marked by the white arrow) to distinguish the malignant tumor (marked by the yellow arrow). Reproduced with permission from reference 24, Copyright © 2013 by John Wiley & Sons, Inc.

1.3.4 Lanthanide-based Nanoparticles as MRI T_2 Contrast Agents

The magnetization of SPIONs saturates at low magnetic fields (around 1.5 T) and the relaxivity r_2 is thus not significantly improved with increasing the magnetic field strength from 0.5 T to 9.4 T.[63] However, the present trend is toward high-field MRI (>3 T), which has the advantages of higher spatial resolution and shorter imaging acquisition times, which offer sensitive and hence potentially earlier diagnosis and clearer imaging.[23, 64] Therefore, it is important to develop high-field contrast agents to take full advantages of high magnetic fields.

Recently, Ln^{3+} ions (Dy^{3+} and Ho^{3+}) have attracted attention for acting as high-field T_2 contrast agents because of their short electronic relaxation time ($\sim 10^{-13}$ s) and relatively large magnetic moment ($\sim 10.6\ \mu_B$), without saturation of the magnetization even at high magnetic fields (up to 9.4 T).[7, 10] Hence, a multitude of studies describe the T_2-weighted performance of Ln^{3+}-based NPs. For instance, van Veggel *et al.* reported that the T_2 relaxivities of Dy^{3+} and Ho^{3+} based NPs increased with increasing particle size (Figure 1.8A).[10] This was as larger NPs possess larger magnetization contributing to higher r_2 values. In addition, the authors also found an effect of surface modification (*i.e.* polyethylene glycol (PEG)) on T_2 relaxivity, namely decreasing the thickness of the surface coating layer increased the r_2 value (Figure 1.8B).[10]

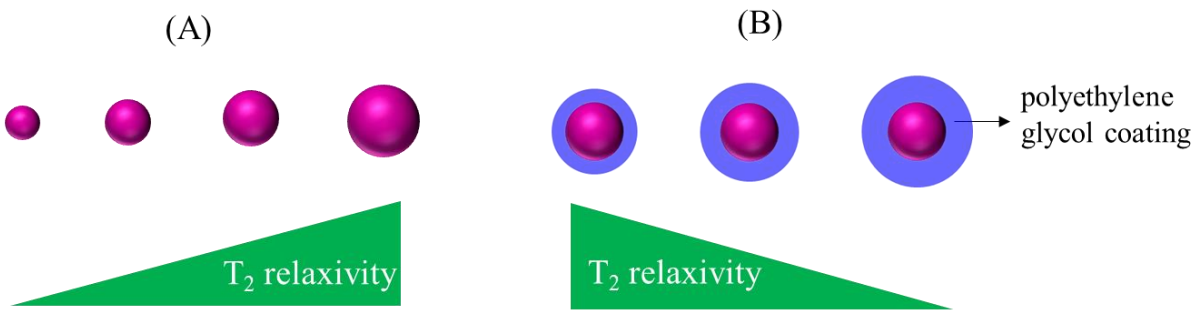

Figure 1.8. Scheme of the effects of particle size (A) and surface coating with polyethylene glycol (B) of Dy^{3+}- and Ho^{3+}-based NPs on T_2 relaxivity. The larger NPs possess larger magnetization contributing to higher T_2 relaxivity (A). Decreasing the thickness of the surface coating layer resulted in higher T_2 relaxivity (B).

1.3.5 Chemical Exchange Saturation Transfer (CEST) Contrast Agents

Chemical Exchange Saturation Transfer (CEST) has emerged as a novel MRI technique that is well suited for molecular imaging studies.[65] The CEST imaging mechanism depends on the reduced detectable water signal after saturating an exchangeable proton on the CEST contrast agents.[66, 67] As shown in Figure 1.9, by applying a proper radiofrequency irradiation field, the

resonance of exchangeable protons of CEST contrast agents is directly saturated. Through chemical exchange, the saturated spins are transferred to the bulk water, thus causing a decrease of the water signal intensity (S_{sat}), which is the source of the signal in the corresponding MR images.[31]

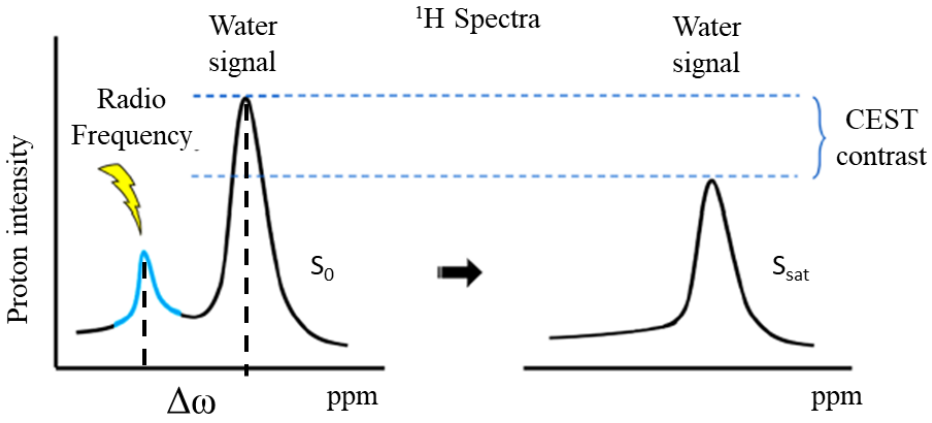

Figure 1.9. Illustration of a CEST process: the exchangeable protons of a CEST contrast agent are selectively saturated using radio frequency (RF) irradiation (shown as blue peak). Because of chemical exchange, the saturated protons are transferred to the bulk water pool, effectively making water signal decreasing (comparing water signal without saturation (S_0) and saturation signal (S_{sat})). Reprinted with permission from reference 31, copyright © 2018, American Chemical Society.

The basic requirement that must be satisfied for CEST imaging to avoid coalescence of the two proton peaks (contrast agent and water) is that the shift difference between the two protons pool (Δω) must be higher than their exchange rate (k_{ex}).[68] CEST agents can be divided into either diamagnetic CEST (diaCEST) and paramagnetic CEST (paraCEST) agents. In general, diaCEST agents are molecules (*e.g.* hydroxy, amine and amide groups) characterized by relatively small Δω values (<10 ppm). Conversely, paraCEST agents are molecules containing a paramagnetic Ln^{3+} ion (*e.g.* Eu^{3+} ion) that endows the systems with large Δω values (up to hundreds of ppm), for instance, Eu^{3+}-DOTA-tetraamide complexes (DOTA=1,4,7,10-tetraazacyclododecane- N,N',N'', N'''-tetraacetic acids).[69, 70] Owing to the large Δω values,

paraCEST agents can eliminate any interference with the background signal eventually present *in vivo*.[71] Moreover, paraCEST agents with a wide variety of chemical and physical properties can be designed by slight modification of the ligand structure or choice of paramagnetic ion.[70] However, the current paraCEST agents have relatively low sensitivity, and a large dose (in mM range) is needed for CEST signals detection.[72] The high concentration requirement makes them difficult to translate to clinical applications. One way to improve the sensitivity of paraCEST contrast agents is increasing the number of exchangeable groups in one agent.[73] Therefore, nanocarriers, with the capacity to load large numbers of exchangeable groups have been developed. Commonly used nanocarriers including liposomes, micelles and proteins, which obtain good contrast images in the μM range.[74, 75] Very recently, it has been reported that mesoporous silica NPs can also be used for paraCEST contrast agents. Botta *et al.* demonstrated that Ln^{3+}-chelates (Ln^{3+}= Eu^{3+}, Tm^{3+} and Tb^{3+}) anchored on the surface of mesoporous silica NPs exhibited higher sensitivity than dendrimers and micelles with the same concentration, and three orders of magnitude higher than that of the corresponding molecule agents (Ln^{3+}-chelates).[76]

1.4 Synthesis of Sodium Lanthanide Fluoride Nanoparticles

In order to fulfill the requirements of MRI *in vivo* applications, ultrasmall NPs (size less than 10 nm)[77] are usually used to avoid blockage of blood vessels, to allow cellular uptake, and to ensure clearance from the body.[6] Among various Ln^{3+}-based NPs, sodium lanthanide fluoride ($NaLnF_4$, Ln=Gd, Dy or Ho) NPs have been frequently studied because of their unique paramagnetic properties, as well as luminescent properties when doped with other optically active Ln^{3+} ions.[78] In general, the most widely used method to prepare $NaLnF_4$ NPs is the thermal decomposition approach.[78, 79] The approach involves the oxygen-free decomposition of organometallic precursors in high-boiling point organic solvents. In general, the organometallic precursors are Ln^{3+}-based acid salts, such as trifluoroacetates [$Ln(TFA)_3$], acetates [$Ln(Ac)_3$] and oleates [$Ln(OA)_3$].[12] Octadecene is the most frequently used high-boiling-point organic solvent to provide a high-temperature environment. Meanwhile, oleic acid and oleylamine containing polar capping groups and long hydrocarbon chains perform as coordinating solvent and surfactant.[80] As is known, $NaLnF_4$ NPs can crystallize in two different phases, namely cubic (α) and hexagonal (β) phases.[81] The thermal decomposition method allows for some control the crystalline phase of the NPs (with specific size regions) and has been demonstrated as highly suitable for the synthesis of core-shell architectures (Figure 1.10).[80,79] However, the preparation of ultrasmall particles of tunable size and phase – at high batch-to-batch and lab-to-lab reproducibility – is still a challenge.

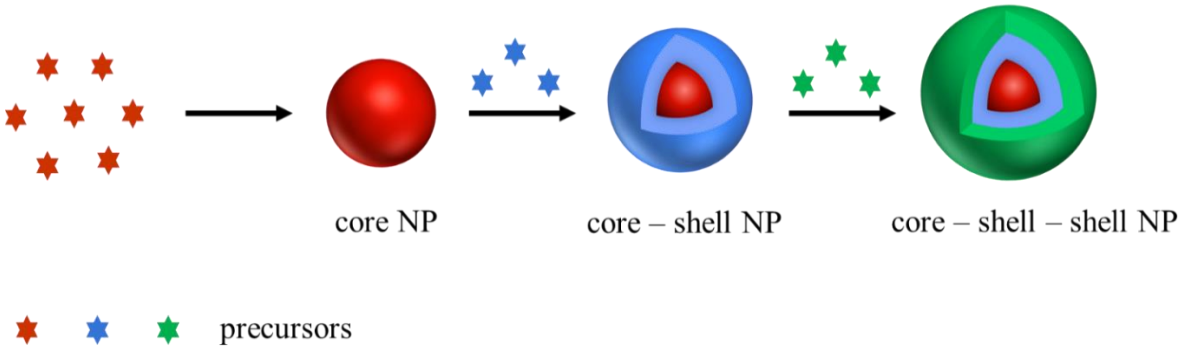

Figure 1.10. Schematic representation of the synthesis of NPs with core-shell architectures (multishells) through injecting different precursors using the thermal decomposition method.

Recently, microwave-assisted thermal decomposition strategies have successfully been applied for the rapid synthesis of ultrasmall $NaLnF_4$ NPs with selective phases and particle compositions.[82-84] Indeed, the microwave-assisted approach provides unique advantages over traditional thermolysis methods reliant on convectional heating, namely, significantly shorter reaction durations, more rigid reaction conditions, and thus a higher degree of reproducibility.[84, 85] However, the simultaneous control of particle size and crystalline phase remains difficult and needs to be addressed to fully take advantage of the microwave-assisted approach. It is expected to overcome these limitations by tuning the reaction parameters (*e.g.* temperature, concentration of precursor).

1.5 Surface Modification of Sodium Lanthanide Fluoride Nanoparticles

The synthesized $NaLnF_4$ NPs are typically capped by surfactant ligands (*e.g.* oleic acid, oleylamine) and hence hydrophobic.[86] Therefore, subsequent modification of the NP surface is a prerequisite to allow for specifically tailored or additional physical, chemical or biological attributes, to be augmented onto the material surface.[87] Various modification strategies have been developed, including ligand oxidation, ligand removal, ligand attraction, ligand exchange, layer-by-layer assembly, and surface silanization (Figure 1.11).[53, 86, 88]

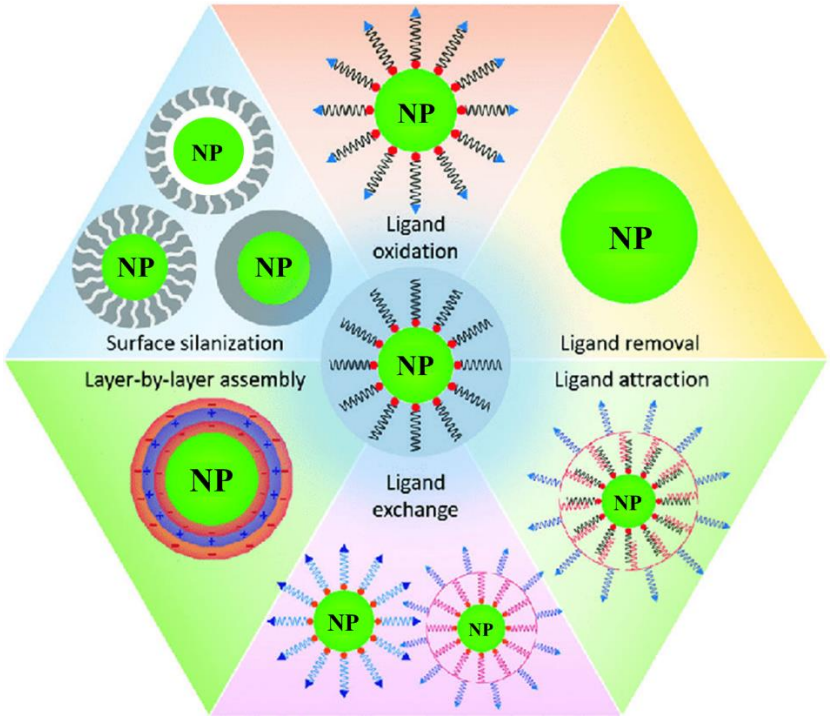

Figure 1.11. A diagram of surface modification methods used to alter the surface chemistry of NPs. Reproduced with permission from reference 88, with permission from The Royal Society of Chemistry.

Among these strategies, ligand exchange is an effective technique to replace the hydrophobic ligands by ligands exhibiting both greater affinity and hydrophilicity. The process is easy to preform and exhibits a negligible effect on the morphology of NPs.[53] The hydrophilic ligands usually used in ligand exchange process include citrate,[86, 87] polyethylene glycol (PEG)

derivatives,[89, 90] poly(acrylic acid) (PAA) derivatives,[90, 91] and phosphate derivatives[90, 92]. Long-term stability of NPs after ligand binding is crucially determined by stability of the ligand coordination with Ln^{3+} ions. Therefore, multidentate ligands (*e.g.* polymers) with a number of coordinating atoms, are preferred over monodentate molecules.[88]

Chapter 2. Objectives

Although various factors influencing MRI relaxometric properties of Ln^{3+}-based NPs have been investigated (as discussed in chapter 1), the effect of the NP crystallinity (*e.g.* $NaLnF_4$) is unknown to date. However, understanding the phase-dependent MRI contrast behaviour is very important for the rational design and manufacturing of NPs as next-generation contrast agents for future *in vivo* biomedical applications.

Therefore, the objective of this thesis was to investigate the effect of the crystalline phase of $NaLnF_4$ NPs on their MRI contrast performance. The specific objectives of this thesis were as follows:

1. Developing a synthetic strategy to prepare a set of $NaGdF_4$ NPs in both cubic and hexagonal phases in the same size range by employing a microwave-assisted approach.

2. Comparing the MRI T_1 relaxivities of cubic and hexagonal $NaGdF_4$ NPs.

3. Preparing $NaDyF_4$ NPs in cubic and hexagonal phases with the same size and comparing their T_2 relaxivities. (Expansion of the observation made on Gd^{3+}-based NPs to other Ln^{3+}-based NPs.)

4. Producing and characterizing alternative material – $NaEuF_4$ NPs – as potential candidates for the preparation of CEST contrast agents.

5. Assessment of the stability of $NaGdF_4$ NPs in different buffer solutions for future *in vivo* experiments.

Chapter 3. Experimental Details and Characterization Techniques

3.1 Chemicals

All reagents were used as received without any further purification. Gadolinium oxide (Gd_2O_3, 99.999%), europium oxide ((Eu_2O_3, 99.999%), dysprosium oxide (Dy_2O_3, 99.9%), and sodium oleate ($NaOOCC_{17}H_{33}$, >97.0%) were purchased from Alfa Aesar. Sodium trifluoroacetate (CF_3COONa, 98%), 1-octadecene ($C_{18}H_{36}$, 90%), oleylamine ($C_{18}H_{37}N$, 70%), trifluoroacetic acid (CF_3COOH, 99%), oleic acid ($C_{18}H_{34}O_2$, 90%), nitrosonium tetrafluoroborate ($NOBF_4$, 98%), sodium citrate dihydrate ($C_6H_9Na_3O_9$, 99%), ammonium fluoride (NH_4F, >98.0%), and poly(acrylic acid) (PAA, #323667) were purchased from Sigma-Aldrich. Ethanol, acetone, hexane, dimethylformamide, chloroform and toluene were of analytical reagent grade.

3.2 Microwave-Assisted Thermal Decomposition Synthesis of $NaGdF_4$ Nanoparticles

$NaGdF_4$ nanoparticles (NPs) were synthesized by employing a modified version of the microwave-assisted approach reported in the literature.[82] The synthetic route for $NaGdF_4$ NPs includes two steps: Preparation of the gadolinium trifluoroacetate precursor and synthesis of $NaGdF_4$ NPs in a microwave reactor.

3.2.1 Synthesis of Gadolinium Trifluoroacetate Precursor

1.25 mmol of Gd_2O_3 were added to a 50 mL three-neck round bottom flask along with 5 mL of distilled water and 5 mL of CF_3COOH (TFA).[93] The resulting mixture was stirred at 85 °C until the solution became transparent, followed by drying at 60 °C overnight in an open

atmosphere. The white powder gadolinium trifluoroacetate (Gd-TFA) was obtained with no further purification (equation 3.1).

$$Gd_2O_3 + 6\ CF_3COOH \xrightarrow[85\ °C,\ reflux]{H_2O} 2\ Gd(OOCCF_3)_3 + H_2O \qquad (3.1)$$

3.2.2 Synthesis of $NaGdF_4$ Nanoparticles

Sodium trifluoroacetate was added to the Gd-TFA precursor with 5 mL of oleic acid, 5 mL of oleylamine and 10 mL of 1-octadecene. The amount of sodium trifluoroacetate varied depending on which crystalline phase was aimed for: 2.5 mmol (1:1 Gd^{3+}:Na^+) were added to synthesized cubic-phase $NaGdF_4$, while 5.0 mmol (1:2 Gd^{3+}:Na^+) were added to obtain the hexagonal phase. This mixture was degassed at 120 °C under vacuum with stirring for 30 min. A gentle flow of nitrogen gas was subsequently introduced to prevent the contents of the flask from coming into contact with the atmosphere.

$$Gd(OOCCF_3)_3 + Na(OOCCF_3) \xrightarrow[\substack{1\text{-octadecene}\\ \text{oleic acid, oleylamine}}]{\substack{300\ °C,\ 1\ s\\ 230\ °C,\ 10\ min}} NaGdF_4 + CO_2 \qquad (3.2)$$

The microwave-assisted synthesis took place in a microwave reactor (Discover CEM, Explorer Hybrid SP) (Figure 3.1, left). In order to obtain $NaGdF_4$ NPs with different sizes, variable volumes of the degassed precursor solution (7-12 mL) were transferred into a 35 mL microwave vessel and purged with nitrogen to keep the solution free from any moisture from the environment. More precisely, for cubic phase $NaGdF_4$ NPs, volumes were 8, 10 and 12 mL for the sizes 6, 7 and 8 nm, while volumes of 7, 9 and 11 mL were used to grow hexagonal phase NPs of same sizes. Subsequently, the vessel was heated with microwave radiation in the reactor under low magnetic stirring at 300 ºC for 1 s and followed by rapid cooling to 230 °C,

the temperature at which the reaction was held for 10 min (Figure 3.1, right). After synthesis, so-prepared oleate-capped $NaGdF_4$ NPs were precipitated with 30 mL of ethanol and collected by centrifugation (6595 rcf for 20 min). The NPs were washed by means of redispersion in 10 mL of toluene and subsequent precipitation by 30 mL acetone (repeated 2 times). The obtained $NaGdF_4$ NPs were stored in 5 mL of hexane.

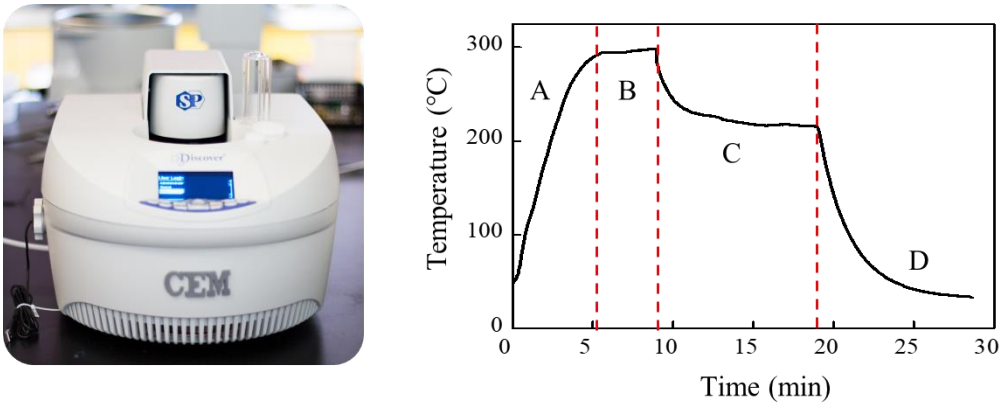

Figure 3.1. Discover CEM microwave reactor (left) and the temperature profile applied for the synthesis of $NaGdF_4$ NPs (right). The temperature profile indicated four stages for NPs formation: (A) precursor decomposition, (B) NP nucleation, (C) NP growth and (D) reaction cooling.

An alternative way to increase the size of NPs was to prepare "core/shell" NPs. The "core/shell" NPs were synthesized by growing a shell with the same Gd-TFA precursor on the "core" $NaGdF_4$ NPs obtained from above step. For the shell growth, the precipitation and washing step of the core-only particles was not performed. Rather, 8 mL of the Gd-TFA was added to the microwave vessel, which contained the already synthesized core-only NPs. Subsequently, the vessel was heated in the microwave reactor to 260 ºC and kept for 5 min (Figure 3.2). After the microwave treatment, the NPs were precipitated and washed as previously described.

To grow even larger NPs, another layer was grown on the obtained NPs to obtain "core/shell/shell" NPs. For the synthesis of the "core/shell/shell" NPs, before washing and

precipitating, 5 mL of the same core precursor was added to 15 mL of the previous solution containing the core/shell NPs. The reaction mixture was heated at 260 ºC in the microwave vessel for 3 min. The products were then washed as described above.

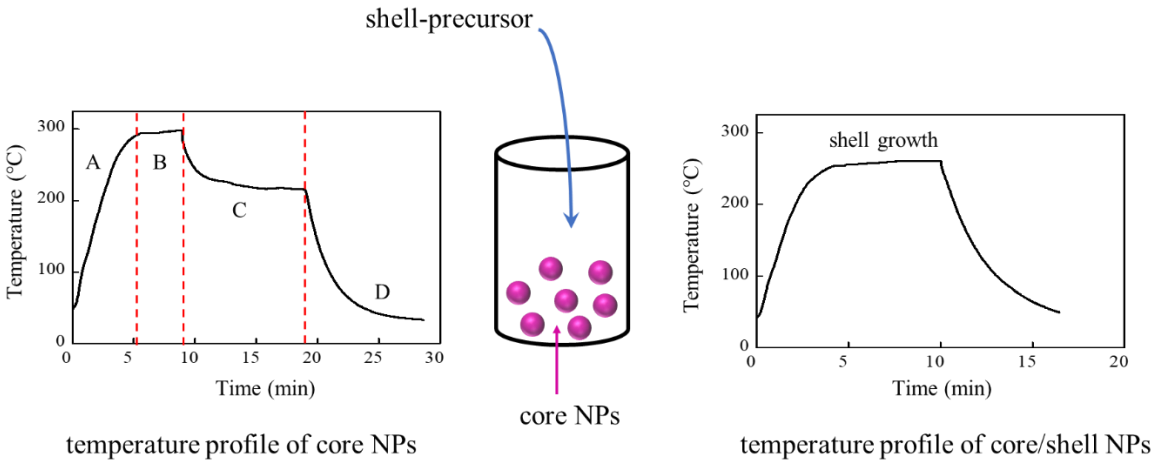

Figure 3.2. Schematic representation of core/shell NPs formation using the microwave temperature profiles.

3.3 Microwave-Assisted Synthesis of Cubic $NaEuF_4$ Nanoparticles

Cubic $NaEuF_4$ NPs were synthesized by the same microwave-assisted approach used for cubic core-$NaGdF_4$ NPs as described above.

3.4 Microwave-Assisted Synthesis of Ultrasmall $NaDyF_4$ Nanoparticles

3.4.1 Synthesis of Dysprosium Oleate Precursor

$NaDyF_4$ NPs were prepared *via* a modified thermal decomposition method described in the literature.[94] In brief, 1.25 mmol of $DyCl_3$ and 3.75 mmol of $NaOOCC_{17}H_{33}$ (Na-OA) were added in a 50 mL three-neck round bottom flask containing a mixture of 2.8 mL of water, 3.8 mL of ethanol, and 6.6 mL of hexanes. The flask was fitted with a reflux condenser and allowed to reflux under vigorous stirring for 2 h at 70 °C. Subsequently, when the reaction

was completed, the upper organic layer containing the $Dy(OOCC_{17}H_{33})_3$ (Dy-OA) was washed three times with 4 mL of a 1:1 water:ethanol mixture in a separatory funnel. After washing, the resulting Dy-OA was kept in hexane solution (equation 3.3).

$$DyCl_3 + 3\ NaOOCC_{17}H_{33} \xrightarrow[\text{water/ethanol /hexane}]{\text{70 °C, 2 h}} Dy(OOCC_{17}H_{33})_3 + 3\ NaCl \qquad (3.3)$$

3.4.2 Synthesis of Ultrasmall $NaDyF_4$ Nanoparticles

10 mL of 1-octadecene was added to the Dy-OA hexane solution and residual hexane was evaporated off at 70 °C under a gentle flow of N_2 with stirring for 15 min. 5 mL of oleic acid, 5 mL of oleylamine and Na-OA were added to the precursor and the mixture was degassed at 100 ºC for 30 min. The amount of Na-OA varied depending on which crystalline phase was aimed for: 1.25 mmol (1:1 Dy^{3+}:Na^+) were added to synthesize cubic-phase $NaDyF_4$, while 5 mmol (1:4 Dy^{3+}:Na^+) were added to obtain the hexagonal phase (equation 3.4).

$$Dy(OOCC_{17}H_{33})_3 + NaOOCC_{17}H_{33} + NH_4F \xrightarrow[\text{1-octadecene, oleic acid, oleylamine}]{\text{100 °C, 1 min; 300 °C, 1 s; 290 °C, 10 min}} NaDyF_4 + NaF \qquad (3.4)$$

Subsequently, 10 mL of the degassed solution was transferred into a 35 mL microwave vessel containing 5 mmol of NH_4F, purged with N_2, and tightly sealed. The reaction took place in the microwave including three stages: first, the reaction solution was heated at 100 ºC for 1 min to dissolve NH_4F, then the solution was heated up to 300 ºC for 1 s, followed by rapid cooling to 290 °C and holding at this temperature for 10 min (Figure 3.3). After the microwave

treatment, the particles were precipitated and washed as previously described in case of $NaGdF_4$. Finally, the washed product was redispersed in 5 mL of hexane for storage.

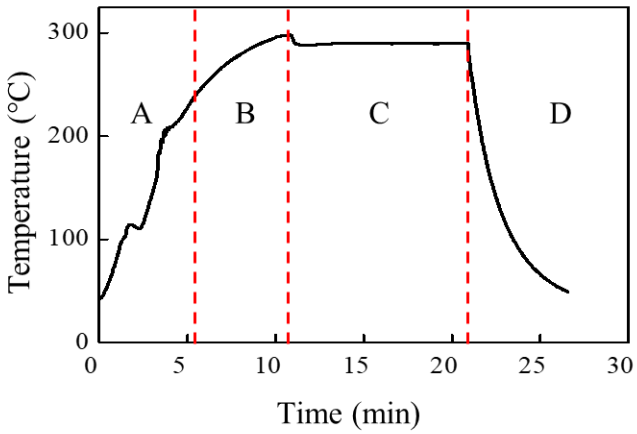

Figure 3.3. Microwave temperature profile for the synthesis of ultrasmall $NaDyF_4$ NPs. The temperature profile indicated four stages for NPs formation: (A) precursor decomposition, (B) NP nucleation, (C) NP growth and (D) reaction cooling.

3.5 Surface Modifications of Nanoparticles Towards Water Dispersibility

3.5.1 Ligand-Free Nanoparticles

15 mL of hexane containing 150 mg of oleate-capped NPs and 15 mL of HCl solution (pH = 1.5) were added to a 125 mL Erlenmeyer flask.[95, 96] The two-phase mixture was stirred overnight at room temperature. Subsequently, the aqueous/organic mixture was poured into a separatory funnel, and the aqueous phase containing the NPs was isolated. The NPs were precipitated with 45 mL of acetone (1:3 aqueous phase:acetone) and centrifuged for 20 min (6595 rcf). The resulting water-dispersible NPs were stored in 5 mL of water.

3.5.2 Surface Modification with $NOBF_4$

100 mg oleate-capped NPs were dispersed in 10 mL hexane, and 100 mg $NOBF_4$ was dissolved in 10 mL dimethylformamide.[86, 97] The mixture was added to a 50 mL round-bottom flask, stirring strongly for 40 min. Subsequently, the NPs were precipitated with 60 mL

chloroform (3:1 chloroform:mixture) and collected by centrifugation (6595 rcf for 20 min). The NPs were washed by means of redispersion in water and subsequent precipitation using acetone (3:1 water:acetone). The obtained BF_4^--stabilized NPs were stored in 5 mL water.

3.5.3 Surface Modification with Citrate Groups

70 mg of oleate-capped NPs was dispersed in 5 mL of hexane and the dispersion was mixed with 5 mL of 0.2 M trisodium citrate buffer (pH = 3). The resulting mixture was stirred for 3h at 40 °C.[48] The aqueous/organic mixture was poured into a separatory funnel, and the aqueous phase now containing the NPs was isolated. The NPs were precipitated with 25 mL of acetone (1: 5 aqueous phase:acetone) and centrifuged for 15 min (6595 rcf). The organic solvent was removed and the recovered solids were re-dispersed in 5 mL of trisodium citrate buffer (pH = 7). The dispersion was stirred for 2 h, followed by three washing steps using water and acetone for precipitation and subsequent centrifugation under aforementioned conditions. The obtained citrate-coated NPs were stored in 5 mL of a 0.02 M sodium citrate solution.

3.5.4 Surface Modification with Poly(acrylic acid)

To prepare PAA-coated NPs, 120 mg PAA were dispersed in 10 mL of ethanol, and 100 mg oleate-capped NPs were dispersed in 5 mL of chloroform. The two solutions were mixed together and stirred overnight.[98] Subsequently, the NPs were precipitated with 120 mL of acetone (8:1 acetone:NP dispersion) and centrifuged for 20 min (6595 rcf). The recovered solids were dispersed in water and washed with acetone twice. The obtained PAA-coated NPs were stored in 5 mL of water.

3.5.5 Dispersion Stability of Cubic $NaGdF_4$ Nanoparticles

5 mg of cubic citrate-coated $NaGdF_4$ NPs dispersed in 1 mL phosphate-buffered saline (PBS) (pH=7.4) and 1 mL pure saline solutions, respectively. For serum incubation, 1 mg of cubic citrate-coated $NaGdF_4$ NPs were added in 1 mL of 10% v/v fetal bovine serum (FBS) PBS solution (or 1 mL FBS saline solution). Particles were incubated with FBS for 1 h at room temperature to allow protein adsorption. All the samples were sonicated for 1 h before performing stability measurements.

3.6 Characterizations Techniques

3.6.1 Transmission Electron Microscopy (TEM)

Size and size distribution of the obtained NPs were determined with a FEI Tecnai G2 Spirit Twin transmission electron microscope (TEM). For TEM observations, samples were dispersed on a Formvar/carbon film supported on a 300-mesh copper grid. Particle sizes of the samples were derived from TEM images using the software ImageJ. The size distribution was calculated analysing 200 particles per each sample. I would like to thank Dr. Riccardo Marin, Nikita Panov and Dr. Emille Martinazzo Rodrigues for TEM measurements.

3.6.2 X-Ray Diffraction (XRD)

Powder X-ray diffraction (XRD) patterns were collected on each sample for the identification of the crystalline phase using a Rigaku Ultima IV diffractometer (Cu Kα, $\lambda = 1.5401$ Å). The scan range was set from 20 to 60° 2θ with a scan speed of 1 degree/min.

3.6.3 Fourier Transform Infrared (FTIR) Spectroscopy

In order to confirm the successful surface modification of the NPs, FTIR spectra were collected in the range 4000-500 cm^{-1} with a Shimadzu 8400s FTIR spectrometer using a pellet

composed of a mixture of dried samples with KBr. All measurements are performed at room temperature, and KBr pellets were prepared as the background.

3.6.4 Thermogravimetric Analyses (TGA)

TGA data was obtained using a TGA Q500 instrument, heating from 30 to 700 °C at a heating rate of 10 °C min^{-1} under air, allowing to estimate the degree of surface modification in each sample. TGA measurements were performed by Dr. Gwenael Chamoulaud at University of Quebec, Montreal.

3.6.5 Dynamic Light Scattering (DLS)

The hydrodynamic diameter and the zeta potential of the water-dispersible NPs were measured with a Malvern Zetasizer Nano-ZS instrument. The measurements were carried out on NPs dispersed in water at room temperature. Three measurements were performed for each sample.

3.6.6 Inductively Coupled plasma Optical Emission Spectroscopy (ICP-OES)

Ln^{3+} ion concentrations were determined with an Agilent ICP-OES spectrometer. Therefore, 10 mg of NPs was added to a mixture of 0.5 mL of concentrated HNO_3 and 1.5 mL of concentrated HCl and heated at 80 °C for 5 h ensuring that all NPs were digested. Flow conditions of the Agilent ICP-OES spectrometer were as follows: nebulizer flow = 0.7 L min^{-1}, plasma flow = 12 L min^{-1}, auxiliary flow = 1 L min^{-1}. ICP-OES measurements were performed by Dr. Anabel Lanterna.

3.6.7 Magnetic Resonance Imaging (MRI) Intensity Measurements

T_1 weighted images were obtained on a 3.0 T MR instrument (MRS-3000 series). All samples were prepared by dispersing the NPs in a 0.02 M citrate solution, and then the NPs dispersions were placed in 200 µL Eppendorf tubes for the measurements. The following instrument

parameters were used: repetition time TR =5000 ms, echo time TE = 16 ms, inversion time TI =51 ms, field of view FOV = 40 cm^2, echo = 16 and slice thickness = 1.5 mm.

3.6.8 MRI Relaxivity Measurements

MRI relaxivity experiments were performed on the same 3.0 T MR instrument (MRS-3000 series). For T_1 measurements, the pulse sequence used was a T_1-weighted fast-spin-echo (FSE) sequence with the following parameters: TR = 5000 ms, TE = 16 ms, twelve inversion times (TI = 50, 100, 150, 250, 350, 500, 800, 1100, 1400, 1700, 2750 and 4000 ms), FOV = 60 cm^2, echo = 16, slice thickness = 5 mm. For T_2 measurements, the used pulse sequence was a T_2-weighted multi-echo-multi-slice (MEMS) sequence with the following parameters: TR = 7500 ms, TE = 64 ms, twelve inversion times (TI = 50, 100, 150, 250, 350, 500, 800, 1100, 1400, 1700, 2750 and 4000 ms), FOV = 60 cm^2, echo = 16, slice thickness = 5 mm.

3.6.9 Time-Domain NMR Relaxivity Measurements

The proton relaxation times of $NaDyF_4$ NPs were measured using a time domain NMR relaxometer. T_1 and T_2 relaxation times were determined at 25 °C on a Bruker Minispec mq20 instrument (Bruker, Billerica, MA) operating at 0.47 T and 20 MHz, being equipped with a temperature control unit. T_1 was obtained with an inversion-recovery sequence. T_2 was obtained by a Carr-Purcell-Meiboom-Gill sequence.

3.6.10 Fluorescence Microscopy

Visible photoluminescence emission spectra were obtained on powdered samples at room temperature with a custom-built microscope (IMA UpconversionTM by PhotonEtc) equipped with an inverted optical microscope (Nikon Eclipse Ti-U), a Nikon Halogen Lamp (IntensiLight 100 W) with a single band DAPI filter cube providing maximum UV excitation at 390 nm, a broad-band camera for colour imaging, a set of galvanometer mirrors, a Princeton

Instruments SP-2360 monochromator/spectrograph, and a Princeton Instruments ProEM EMCCD camera for detection of the visible emission. A 400 nm long-pass filter (Thorlabs) was inserted at the emission side of the DAPI cube in order to allow for the detection of the visible emission, while cutting off the excitation wavelength.

Chapter 4. Cubic versus Hexagonal – Effect of Host Crystallinity on the T_1 Shortening Behaviour of $NaGdF_4$ Nanoparticles

This chapter was published in Nanoscale: N. Liu, R. Marin, Y. Mazouzi, G. O. Cron, A. Shuhendler, and E. Hemmer, *Nanoscale*, 2019, 11, 6794-6801.

4.1 Introduction

$NaGdF_4$ NPs have been widely studied as MRI T_1 contrast agents, and increasing research efforts have been undertaken in order to describe their T_1-weighted performance.[41, 46, 48, 56, 57, 99] However, to date, there has been no attention paid to the effect of the crystalline phase of $NaGdF_4$ NPs on T_1 relaxivity. $NaGdF_4$ can crystallize either in the cubic α- (*Fm*-3*m*) or hexagonal β-phase (*P*-6) (Figure 4.1), which feature different mass densities ρ (ρ_{cubic} = 5.06 g cm^{-3} versus $\rho_{hexagonal}$ = 5.61 g cm^{-3})[41] and Gd^{3+} ion distributions over the lattice.[81] Therefore, the number of Gd^{3+} ions in a single NP of either the hexagonal or the cubic phase differs, as does the number of Gd^{3+} ions on the NP surface. The different arrangement of Gd^{3+} ions in the particle ensemble is expected to have an influence on r_1, and insights in these aspects will be valuable for the development of more efficient NP-based MRI contrast agents.

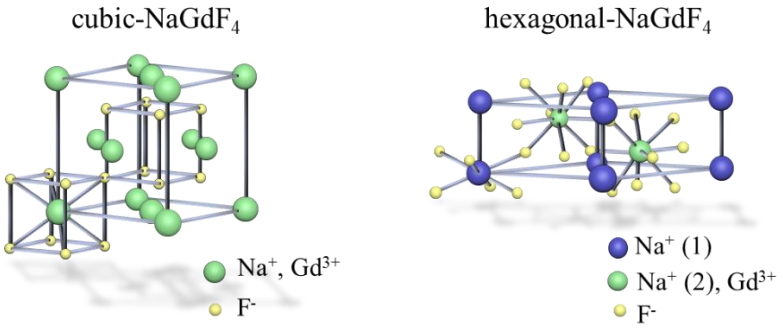

Figure 4.1. Crystal structures of cubic and hexagonal $NaGdF_4$. Redrawn from reference 81.

In order to assess the effect of crystallinity of $NaGdF_4$ NPs on T_1 relaxivity, a set of NPs with same sizes in both phases should be prepared. However, the simultaneous fulfilment of these size and phase requirements is challenging, because the two polymorphs of $NaGdF_4$ commonly have different ranges of stability in terms of NP size, namely cubic NPs are stable in small particle size while hexagonal NPs prefer in larger particle size.[78, 80] To overcome this limitation, a synthetic strategy that grants access to NPs of the two polymorphs in the same size range was developed. Having NPs with the same sizes and surface modification in different phases on hand, the effect of the crystalline phase on the T_1 relaxivity was assessed.

4.2 Results and Discussion

4.2.1 Microwave-Assisted Synthesis of $NaGdF_4$ Nanoparticles

A set of ultrasmall $NaGdF_4$ NPs (6.1 - 8.2 nm) in both cubic and hexagonal polymorphs that are truly comparable in terms of size were obtained by employing a modified version of the microwave-assisted approach for the rapid synthesis of cubic Ln^{3+}-doped $NaGdF_4$ NPs.[82] Here, the synthesis parameters were developed to result in methodology allowing us to independently vary (i) the NP crystalline phase by adjusting the molar ratio of Na^+ to Gd^{3+} ions in the reaction mixture and (ii) the NP size by changing the volume of the reaction mixture. X-ray diffraction (XRD) patterns of cubic and hexagonal oleate-capped $NaGdF_4$ NPs are shown in Figure 4.2. The XRD patterns confirmed that phase control *via* the modified synthesis approach allowed the selective growth of phase-pure $NaGdF_4$ NPs in the cubic and hexagonal phases. For both sample series (hexagonal and cubic), characteristic broadening of the XRD reflexes was observed with decreasing particle size.

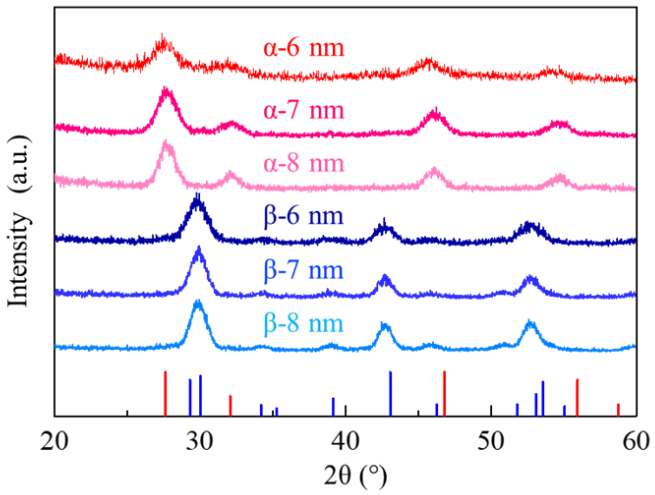

Figure 4.2. XRD patterns of cubic and hexagonal oleate-capped $NaGdF_4$ NPs of various sizes. References: red line – cubic $NaGdF_4$ (PDF card no. 00-027-0697), blue line – hexagonal $NaGdF_4$ (PDF card no. 01-080-8787). [N. Liu et al. Nanoscale, 2019, 11, 6794.] - Reproduced by permission of The Royal Society of Chemistry.

As known, in the crystal structure of cubic $NaGdF_4$, Na^+ and Gd^{3+} cations are randomly distributed in the cationic sublattice, while the hexagonal phase possesses relatively fixed ion sites for both Na^+ or Gd^{3+} (Figure 4.1).[78] It has been reported that pure cubic $NaLnF_4$ could be obtained at a relatively low temperature and low ratio of Na^+ to Ln^{3+} within a relatively short reaction time, while the hexagonal NP was formed under the reverse conditions.[80, 100] This is because the transformation from the cubic phase to the hexagonal phase is of a disorder-to-order character with respect to the cations.[78] In this work, such favoured formation of the hexagonal phase in the presence of excess Na^+ ions is in agreement with previous work on the growth mechanism of $NaLnF_4$ NPs.[78, 80, 101]

Morphology and size of the synthesized $NaGdF_4$ NPs were observed by transmission electron microscopy (TEM). As shown in Figure 4.3, the NPs were well monodisperse with a quasi-spherical shape. Importantly, both cubic (A1-3) and hexagonal (B1-3) NPs featured sizes that

were comparable in pairs, allowing to reliably assess the effect of one polymorph over the other on the MRI contrast agent performance.

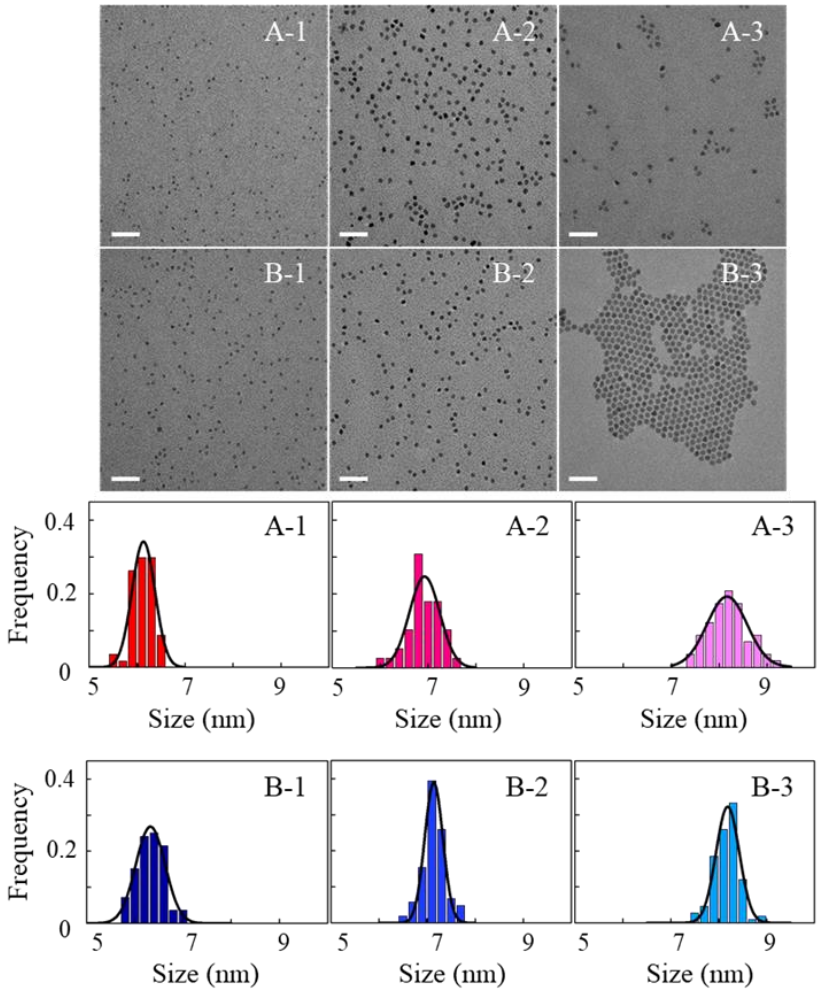

Figure 4.3. TEM micrographs (top, scale bars are 50 nm) and size distribution histograms (bottom) of oleate-coated $NaGdF_4$ NPs crystallized in the cubic α- (A) and hexagonal β-phase (B) with sizes of (A-1) 6.07 ± 0.18 nm, (A-2) 6.93 ± 0.63 nm, (A-3) 8.16 ± 0.42 nm, (B-1) 6.32 ± 0.30 nm, (B-2) 7.14 ± 0.19 nm, (B-3) 8.19 ± 0.24 nm. Black solid lines are Gaussian fitting curves of the size distributions. [N. Liu et al. Nanoscale, 2019, 11, 6794.] - Reproduced by permission of The Royal Society of Chemistry.

Together, XRD and TEM measurements underline that the microwave-assisted approach allows to tune the size and crystalline phase of $NaGdF_4$ NPs at the sub-10-nm realm in a straightforward manner. This was the first time that such particle size and crystalline phase

control in a microwave synthetic route was reported. It is also expected to open exciting possibilities for the investigation of the independent effect of size and crystalline phase on other physical properties (*e.g.* magnetic property) of ultrasmall fluoride NPs.

4.2.2 Citrate-Coated $NaGdF_4$ Nanoparticles

Dispersibility of a contrast agent in aqueous media is a prerequisite for MRI applications. Therefore, the obtained oleate-capped $NaGdF_4$ NPs were transferred to water using trisodium citrate. Citrate groups were chosen as a model capping agent that has already successfully been applied in other Gd^{3+}-based NP MRI studies.[48, 102, 103] Citrate coating was confirmed by Fourier transform-infrared (FTIR) spectroscopy. As shown in Figure 4.4, the FTIR spectra of both cubic and hexagonal $NaGdF_4$ NPs exhibited bands at 3400 and 1600 cm^{-1} that correspond to the stretching and asymmetric stretching vibrations of –OH and $–COO^-$ groups in citrate.[102] This indicated successful coating of all samples with citrate molecules.

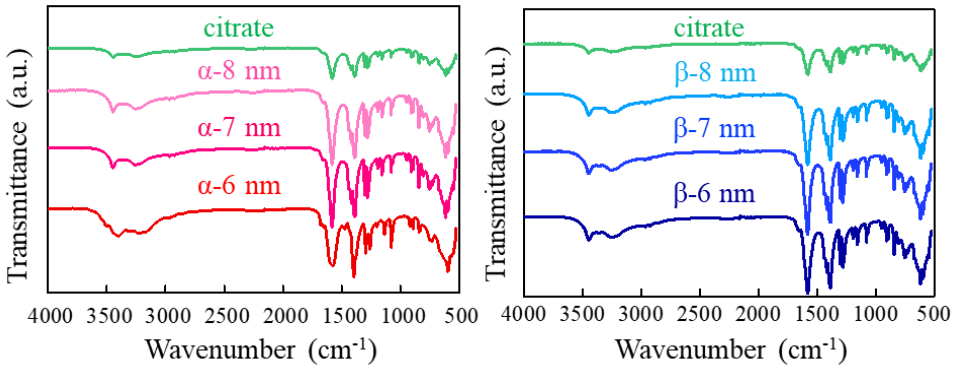

Figure 4.4. FTIR spectra of citrate-coated cubic (α) and hexagonal (β) $NaGdF_4$ NPs of three different sizes as well as sodium citrate dihydrate used as reference. [N. Liu et al. Nanoscale, 2019, 11, 6794.] - Reproduced by permission of The Royal Society of Chemistry.

The zeta (ζ)-potential of each sample was determined to investigate the colloidal stability of the citrate-coated $NaGdF_4$ NP dispersions in water. As shown in Table 4.1, cubic and hexagonal NPs featured similar negative ζ-potential values, which is related to the presence of

citrate carboxylic groups not involved in the coordination with surface Gd^{3+} ions. According to literature values, the ζ-potentials observed indicate that $NaGdF_4$ NPs in both polymorphs should exhibit colloidal stability.[102] Moreover, the TEM images of citrate-coated NPs are shown in Figure 4.5, confirming that these particles were well-dispersed after coating with citrate groups.

Table 4.1. Zeta (ζ)-potential, amount of citrate (m_{cit}), hydrodynamic diameter (d_H), and polydispersity index (PDI) values obtained for cubic and hexagonal $NaGdF_4$ NPs (m_{cit} and d_H will be discussed below).

size (nm)	ζ-potential (mV) [a]		m_{cit} (mass%)[b]		d_H (nm) [PDI][§]	
	cubic	**hexagonal**	**cubic**	**hexagonal**	**cubic**	**hexagonal**
6	-16.4 ± 0.5	-15.0 ± 0.3	29.6 ± 0.3	29.0 ± 0.3	13.1 [0.37]	8.7 [0.47]
7	-12.6 ± 0.4	-21.5 ± 0.4	29.3 ± 0.3	29.6 ± 0.3	16.7 [0.23]	9.6 [0.56]
8	-18.6 ± 0.5	-23.0 ± 0.6	28.8 ± 0.3	28.8 ± 0.3	18.8 [0.25]	10.1 [0.54]

[a] ζ-potential results are expressed as the mean value ± standard deviation as obtained from three measurements on aqueous dispersions of citrate-coated $NaGdF_4$ NPs. [b] Errors given as ± are the TGA instrumental error (0.01 %). [c] d_H values were obtained from number-weighted DLS size distributions.

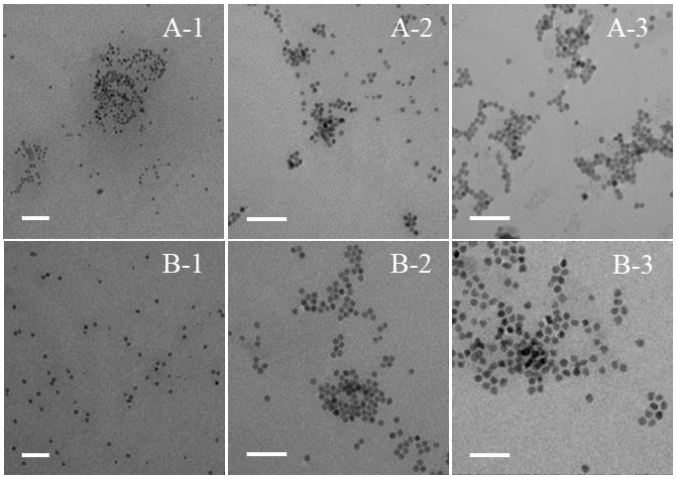

Figure 4.5. TEM images of citrate-coated $NaGdF_4$ NPs crystallized in the (A) cubic and (B) hexagonal polymorph of three different sizes (6, 7, and 8 nm). Scale bars are 50 nm. [N. Liu et al. Nanoscale, 2019, 11, 6794.] - Reproduced by permission of The Royal Society of Chemistry.

4.2.3 MRI Relaxivity Studies of Citrate-Coated $NaGdF_4$ Nanoparticles

MRI T_1 and T_2 relaxivities (r_1 and r_2) of citrate-coated $NaGdF_4$ were measured at 3 T. The relaxivities were extracted from the slopes of the linear fits of the relaxation rates R_1 and R_2 (= $1/T_1$ and $1/T_2$) against the molar concentration of Gd^{3+} ions of the tested NP dispersions as obtained from inductively coupled plasma optical emission spectroscopy (ICP-OES) (Figure 4.6). The obtained r_1 and r_2 values are listed in Table 4.2. Interestingly, r_1 values for cubic NPs (ranging from 16.81 to 13.39 $mM^{-1}s^{-1}$) were approximately twice as large as the values found for their hexagonal analogues (9.91 to 6.55 $mM^{-1}s^{-1}$) over the studied size range from 6 to 8 nm. Of note, the highest r_1 value from the smallest NPs in the cubic phase was 6 times larger compared with the clinical standard Gd-DOTA (2.8 $mM^{-1}s^{-1}$),[104] and approximately twice as large as 3 nm hexagonal PEG-coated $NaGdF_4$ NPs (8.93 $mM^{-1}s^{-1}$) reported previously.[56]

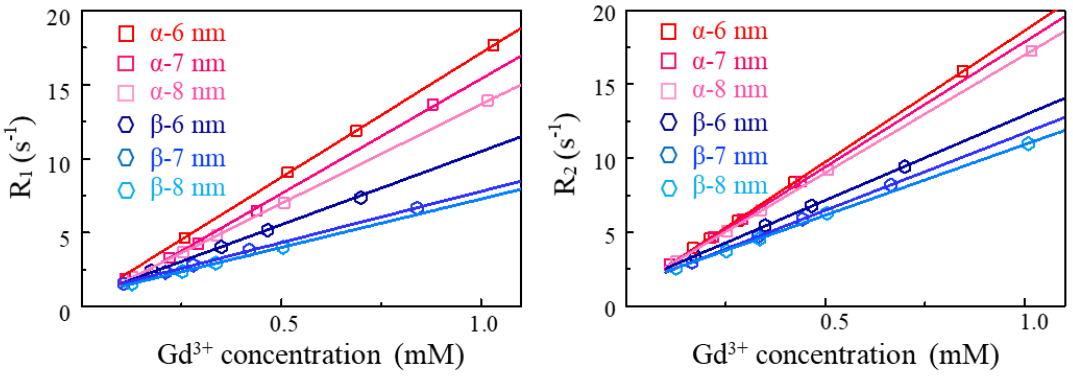

Figure 4.6. Relaxation rates R_1 (left) and R_2 (right) (= $1/T_1$ and $1/T_2$) of water protons plotted against the molar concentration of Gd^{3+} for citrate-coated cubic (α) and hexagonal (β) $NaGdF_4$ NPs of three different sizes at 3 T. Solid lines are linear fits. Red data points and fits stand for cubic NPs, while blue data points and fits stand for hexagonal NPs. [N. Liu et al. Nanoscale, 2019, 11, 6794.] - Reproduced by permission of The Royal Society of Chemistry.

Table 4.2. Relaxivity values r_1 and r_2 of cubic and hexagonal $NaGdF_4$ NPs at 3 T. Relaxivity values and the associated errors were obtained from the linear fitting procedure of the data sets reported in Figure 4.6. The errors associated to the r_2/r_1 ratios were obtained with standard error propagation formulas.

size (nm)	r_1 ($mM^{-1}s^{-1}$)		r_2 ($mM^{-1}s^{-1}$)		r_2/r_1	
	cubic	hexagonal	cubic	hexagonal	cubic	hexagonal
6	16.81 ± 0.09	9.91 ± 0.12	17.76 ± 0.03	11.52 ± 0.08	1.06 ± 0.05	1.16 ± 0.04
7	15.51 ± 0.38	6.93 ± 0.07	16.95 ± 0.12	10.47 ± 0.05	1.09 ± 0.03	1.51 ± 0.01
8	13.39 ± 0.08	6.55 ± 0.06	15.97 ± 0.06	9.56 ± 0.10	1.19 ± 0.01	1.46 ± 0.02

Noteworthy, high relaxivity agents are generally considered beneficial as they can allow for the administration of lower doses, ultimately contributing to lower toxicity[105]. Thus, the higher r_1 values featured by the cubic $NaGdF_4$ NPs indicate that these particles bring superior magnetic properties – while exhibiting comparable size, morphology and dispersibility behaviour – rendering them more promising candidates as T_1 contrast agents compared to the hexagonal NPs. However, good contrast enhancement ability does not only require a high r_1 value, but also a small r_2/r_1 ratio. Low r_2/r_1 ratio provides for higher signal-to-noise and, ultimately, more robust contrast enhancement in T_1-weighted images. Comparison between the two polymorphs showed that the r_2/r_1 values for cubic $NaGdF_4$ NPs were smaller (and closer to 1) than those of the hexagonal counterparts, which further corroborates the observation that cubic $NaGdF_4$ NPs exhibit advanced performance as MRI T_1 contrast agents.[46] This is also confirmed by T_1-weighted images shown in Figure 4.7, the smallest cubic NP (6 nm) presenting the brightest signal.

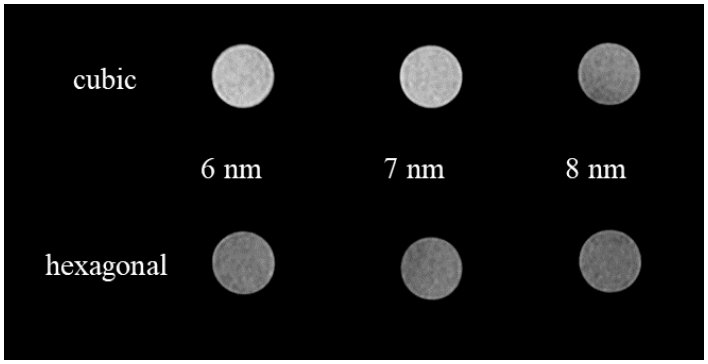

Figure 4.7. T_1-weigthed images of $NaGdF_4$ NPs coated with citrate of different size and crystalline phase obtained at 3 T (Gd^{3+} concentration as determined by ICP: 0.125 mM). [N. Liu et al. Nanoscale, 2019, 11, 6794.] - Reproduced by permission of The Royal Society of Chemistry.

As mentioned before, higher volumetric mass density (as in case of the hexagonal crystalline structure) comes along with a larger number of Gd^{3+} surface ions per NP. This may trigger the expectation of higher r_1 relaxivities due to the increased number of Gd^{3+} surface ions available to interact with protons of the surrounding water molecules. However, this is in contrast to the experimental MRI relaxivity results. Therefore, based on the Gd^{3+} ion concentration as obtained by ICP-OES, NP size obtained by TEM and crystallographic data for both polymorphs, we estimated the total number of Gd^{3+} surface ions for cubic and hexagonal NPs (Table 4.3 and Figure 4.8). Subsequently, the overall surface and the total number of Gd^{3+} surface ions could be calculated (considering as "surface" of each NP a layer thick enough to contain one unit cell, *i.e.* 0.5 nm). Based on the calculations in Table 4.3, though the number of Gd^{3+} ions in one hexagonal particle is more than cubic particle, there are fewer NPs in the hexagonal samples. The resulting total numbers of Gd^{3+} surface ions in both phases $NaGdF_4$ NPs are shown in Figure 4.9.

Table 4.3. Calculation of the total number of Gd^{3+} surface ions in cubic and hexagonal $NaGdF_4$ NPs.

	formula	cubic $NaGdF_4$			hexagonal $NaGdF_4$		
XRD PDF card number		00-027-0697			01-080-8787		
Number of Gd^{3+} per formula, $N_{Gd/formula}$		1 ($NaGdF_4$)			1.5 [$(NaGdF_4)_{1.5}$]		
Number of formulas, Z		2			1		
a (nm)		0.552			0.603		
b (nm)		0.552			0.603		
c (nm)		0.552			0.361		
Volume of unit cell, V_{cell} (nm^3)	$V_{cell} = a \times b \times c$	0.168			0.113		
Diameter of NP, d (nm)		6.1	6.9	8.2	6.3	7.1	8.2
Volume of NP, V_{NP} (nm^3)	$V_{NP} = \frac{4}{3}\pi\left(\frac{d}{2}\right)^3$	118.85	172.01	288.70	130.92	187.40	288.70
Surface of NP, S_{NP} (nm^2)	$S_{NP} = \pi d^2$	116.9	149.57	211.24	124.69	158.37	211.24
Thickness of NP shell†, dR (nm)	$dR = 0.5$ 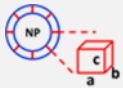						
Volume of shell, V_{shell} (nm^3)	$V_{shell} = \frac{4}{3}\pi\left[\left(\frac{d}{2}\right)^3 - \left(\frac{d}{2} - dR\right)^3\right]$	49.39	64.47	93.26	52.97	68.55	93.26
Number of Gd^{3+} in one NP, $N_{Gd/NP}$	$N_{Gd/NP} = \frac{V_{NP}}{V_{cell}} \times Z \times N_{Gd/Formula}$	1415	2048	3437	1727	2472	3808
Number of Gd^{3+} in the shell of one NP (~ Gd^{3+} surface ions per NP), $N_{Gd/shell}$	$N_{Gd/shell} = \frac{V_{shell}}{V_{cell}} \times Z \times N_{Gd/Formula}$	588	767	1110	699	904	1230
Gd^{3+} concentration determined by ICP-OES‡, C_{mass} (ppm or mg/L)		100	100	100	100	100	100
Gd^{3+} molar concentration, C_{Gd} (mmol/L)	$C_{Gd} = \frac{C_{mass}}{M_{Gd}}$	0.64	0.64	0.64	0.64	0.64	0.64
Total number of Gd^{3+}, N_{Gd} ($\times 10^{20}$/L)	$N_{Gd} = C_{Gd} \times 6.022 \times 10^{23} mol^{-1}$	3.83	3.83	3.83	3.83	3.83	3.83

Table 4.3 (continued). Calculation of the total number of Gd^{3+} surface ions in cubic and hexagonal $NaGdF_4$ NPs.

	formulas	cubic $NaGdF_4$			hexagonal $NaGdF_4$		
Total number of NPs, N_{NP} ($\times 10^{17}$/L)	$N_{NP} = \frac{N_{Gd}}{N_{Gd/NP}}$	2.71	1.87	1.11	2.22	1.55	1.01
Total number of Gd^{3+} surface ions, $N_{Gd/surface}$ ($\times 10^{20}$/L)	$N_{Gd/surface} = N_{Gd/shell} \times N_{NP}$	1.64	1.48	1.28	1.60	1.45	1.28

† 0.5 nm were chosen as approximate dimension of the unit cells yielding a one-unit-cell thick surface layer. ‡ For each type of NPs, five dispersions with different NP concentrations were analysed by ICP OES. Yet, here, exemplarily calculations are provided for a concentration of 100 ppm. Identical calculations can be performed for any concentration, including those concentrations obtained by ICP-OES on the samples under investigation, in order to obtain the curves plotted in Figure 4.9.

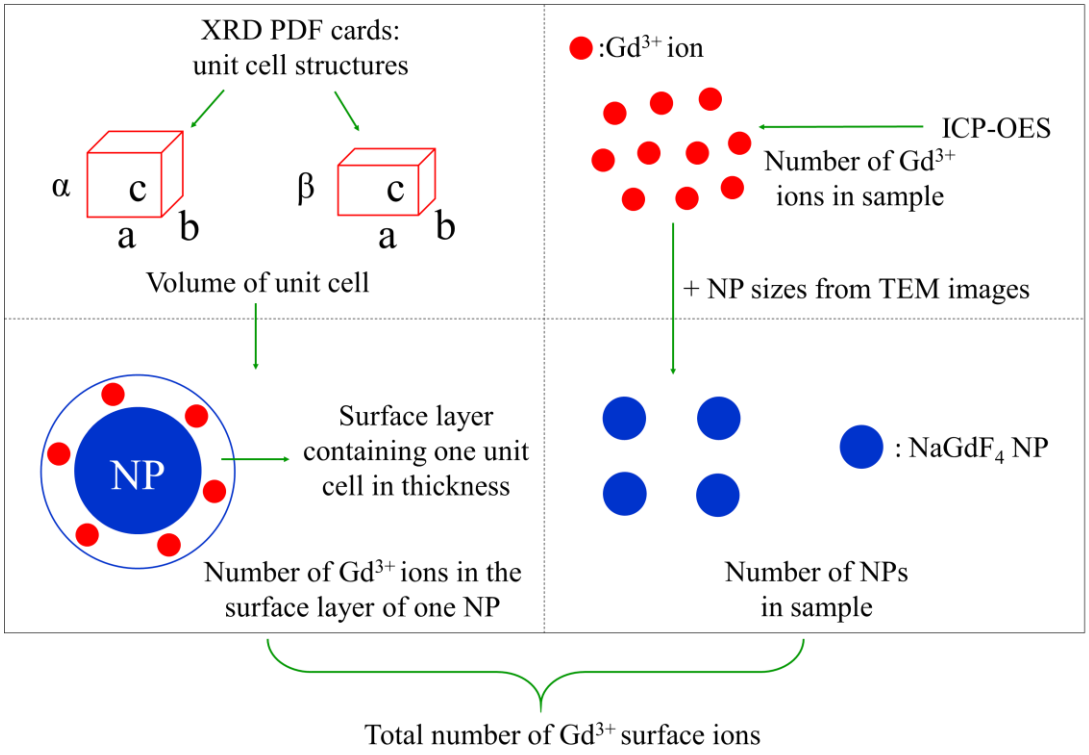

Figure 4.8. Schematic representation for the estimation of the total number of Gd^{3+} surface ions. [N. Liu et al. Nanoscale, 2019, 11, 6794.] - Reproduced by permission of The Royal Society of Chemistry.

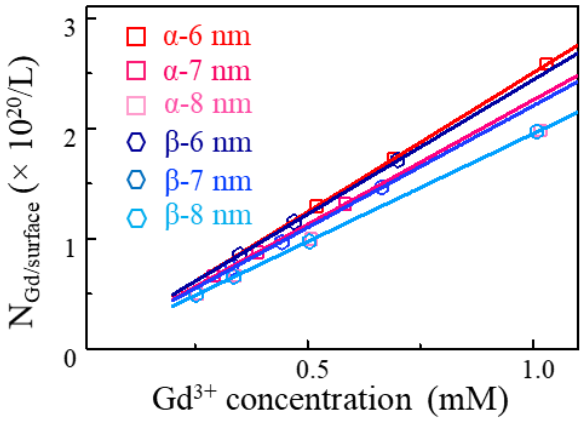

Figure 4.9. Calculated total number of Gd^{3+} surface ions plotted against the Gd^{3+} molar concentration for cubic and hexagonal polymorphs of three different sizes. Red data points and curves stand for cubic NPs, while blue data points and curves stand for hexagonal NPs (data points represent samples investigated in this study). Note that that the two curves obtained for the largest set of NPs perfectly overlap. [N. Liu et al. Nanoscale, 2019, 11, 6794.] - Reproduced by permission of The Royal Society of Chemistry.

As obvious from Figure 4.9, the slopes of the curves obtained using the formulas given in Table 4.3 were very similar for cubic and hexagonal polymorphs. In fact, when the NP size increased to 8 nm, the curves for both polymorphs perfectly overlapped. This indicates that dispersions containing cubic or hexagonal $NaGdF_4$ NPs have very similar total numbers of Gd^{3+} surface ions. Consequently, differences in material density for cubic and hexagonal $NaGdF_4$ cannot be the sole aspect contributing to the observed phase-induced variation of r_1. An important contributing factor in r_1 modulation may be the influence of the crystalline phase of $NaGdF_4$ NPs on the surface modification of NPs with citrate groups, which can affect the interaction between Gd^{3+} surface ions and protons from the surrounding water molecules.[106]

In order to elucidate the observed differences in the enhanced contrast capability of $NaGdF_4$ NPs in cubic and hexagonal polymorphs, the Solomon–Bloembergen–Morgan theory was employed.[107, 108] According to this theory, longitudinal relaxivity (r_1) enhancement of water protons induced by paramagnetic NPs is the sum of the individual contributions from inner

sphere (IS) and outer sphere (OS) water molecules (Figure 4.10). Water molecules that are directly bound to the NP surface account for the IS, while those that are diffusing in close proximity account for the OS contributions. The IS longitudinal relaxivity can be described by the following Solomon–Bloembergen equation (4.1) – (4.4):[50]

$$r_1^{IS} \propto \frac{1}{T_{1m}} \tag{4.1}$$

$$R^{IS} = \frac{2}{15}\left(\frac{\mu_0}{4\pi}\right)^2 {\mu_{eff}}^2 \frac{{\gamma_I}^2}{r^6}\left[\frac{3\tau_{C1}}{1+\omega_I{}^2{\tau_{C1}}^2} + \frac{7\tau_{C1}}{1+\omega_S{}^2{\tau_{C1}}^2}\right] + \frac{2}{5}\left(\frac{\mu_0}{4\pi}\right)^2 \left(\frac{{\mu_{eff}}^2 B_0}{3K_B T}\right)^2 \frac{{\gamma_I}^2}{r^6}\left[\frac{3\tau_{C2}}{1+\omega_I{}^2{\tau_{C2}}^2}\right] \tag{4.2}$$

$${\tau_{C1}}^{-1} = {\tau_S}^{-1} + {\tau_R}^{-1} + {\tau_M}^{-1} \tag{4.3}$$

$${\tau_{C2}}^{-1} = {\tau_R}^{-1} + {\tau_M}^{-1} \tag{4.4}$$

where T_{1m} is the relaxation time of the water proton, μ_0 is the permeability of vacuum, μ_{eff} is the effective magnetic moment of the Gd^{3+} ions, γ_I is the proton gyromagnetic ratio, r is the distance between Gd^{3+} and the Gd^{3+}-bound water protons, ω_I and ω_S are the angular precession frequencies of proton and electron, respectively, B_0 is the intensity of the static magnetic field, k_B is the Boltzmann constant, τ_{C1} and τ_{C2} are the correlation times of dipolar interaction and Curie contribution, τ_S is the electronic relaxation time, τ_M is the residence lifetime of the bound water, and τ_R is the rotational correlation time.

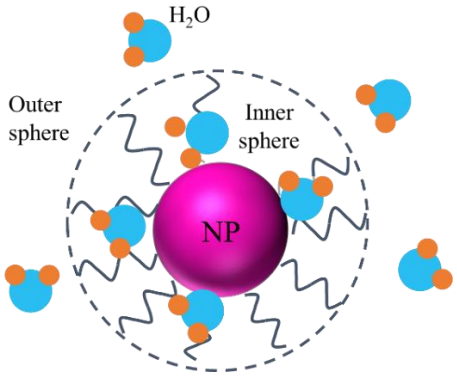

Figure 4.10. Schematic representation of inner sphere and outer sphere contributions of water molecules around the NP.

We here consider cubic and hexagonal $NaGdF_4$ NPs paired according to their size as determined by TEM – 6, 7, and 8 nm, respectively. Thus, from equation (4.2) and (4.3), we can just consider the effects of μ_{eff} and τ_R when comparing the obtained r_1 values.[23, 50] Further, these equations also show that larger μ_{eff} and τ_R values will contribute to larger T_{1m} values resulting in higher r_1 values (equation 4.1). Consequently, these two parameters, μ_{eff} and τ_R, will be addressed in more detail below. Recently, it has been demonstrated that the magnetization (M_z) value of cubic $NaLnF_4$ NPs was higher than the one featured by their hexagonal counterparts.[109] As M_z and μ_{eff} are correlated through magnetic susceptibility (χ), this indicates a larger μ_{eff} value for the cubic phase NPs than for the hexagonal polymorph.[110] In turn, a larger μ_{eff} value will contribute to larger r_1 (equation 4.2). Our observations are in line with this theory, as determined r_1 values of cubic NPs were twice as large as the values of their hexagonal analogues.

The rotational correlation time, τ_R, of the NPs can be calculated from the classical Debye–Stokes equation:[50]

$$\tau_R = \frac{4\pi\eta a^3}{3TK_B} \tag{4.5}$$

with η being the viscosity of the medium and a the hydrodynamic radius of the NPs. Accordingly, a larger hydrodynamic radius results in a larger τ_R value. The hydrodynamic diameter d_H, and therewith a, is accessible *via* dynamic light scattering (DLS) measurements. DLS results obtained on the three size pairs of $NaGdF_4$ NPs in both crystalline phases are shown in Figure 4.11 and are summarized in Table 1. This shows that, despite exhibiting the same TEM size, the d_H of cubic NPs is larger than that of hexagonal NPs. This polymorph-dependent increase in d_H points towards larger τ_R values (equation 4.5) in case of cubic $NaGdF_4$NPs, and hence can explain the observed larger r_1 values (equations 4.1-4.4).

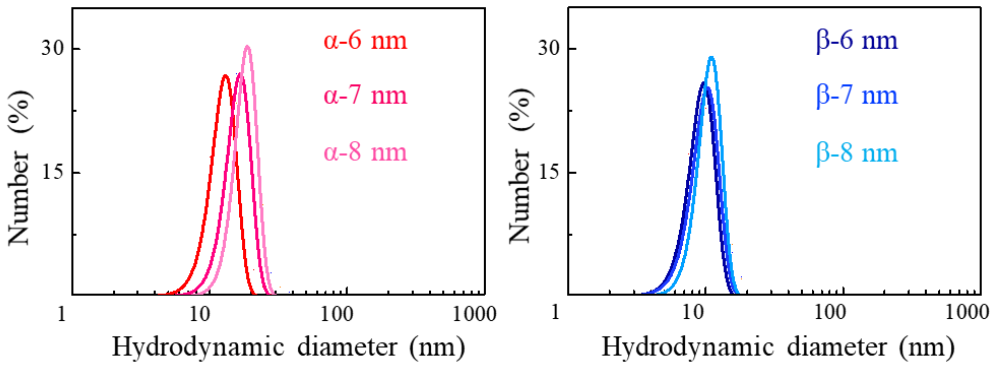

Figure 4.11. DLS curves of citrate-coated cubic (α) and hexagonal (β) $NaGdF_4$ NPs dispersed in 0.02 M citrate solution. These number-weighted DLS size distributions provide information about the size of those NPs that constitute the major part of the dispersion. [N. Liu et al. Nanoscale, 2019, 11, 6794.] - Reproduced by permission of The Royal Society of Chemistry.

In this study, citrate groups have been attached to the surface of all samples to ensure water dispersibility. It has been reported that the amount of surface-bound citrate directly correlates with the size of the hydrodynamic diameter, with less citrate groups resulting in larger d_H values.[106, 111] This was ascribed to a reduced hydrophilicity in terms of adsorption of water molecules in the form of multilayers, likely because of the outward exposure of $–CH_2$ groups in citrate molecules. The amount of citrate in each of our $NaGdF_4$ sample was determined by thermogravimetric analysis (TGA). As shown in Figure 4.12, the thermograms of cubic and hexagonal NPs were characterized by a similar trend. Specifically, two weight losses can be observed: the first at around 170 °C, which was assigned to loss of water, and the second at around 310 °C attributed to the decomposition of citrate.[103] Yet, no significant variation in the amount of citrate (m_{cit}) was found among the six samples, all of them accounting for approximately 29 mass% of the sample weight (Table 4.1). Such relatively high citrate amount indicates excess citrate in all samples, particularly, when expecting a monolayer of citrate being formed on the surface of the NPs.[112, 113] Despite this overestimation, the amount of citrate

on the surface of a single NP (m_{cit}/NP) was determined for each sample based on its total mass of citrate, total mass of $NaGdF_4$, and number of NPs.

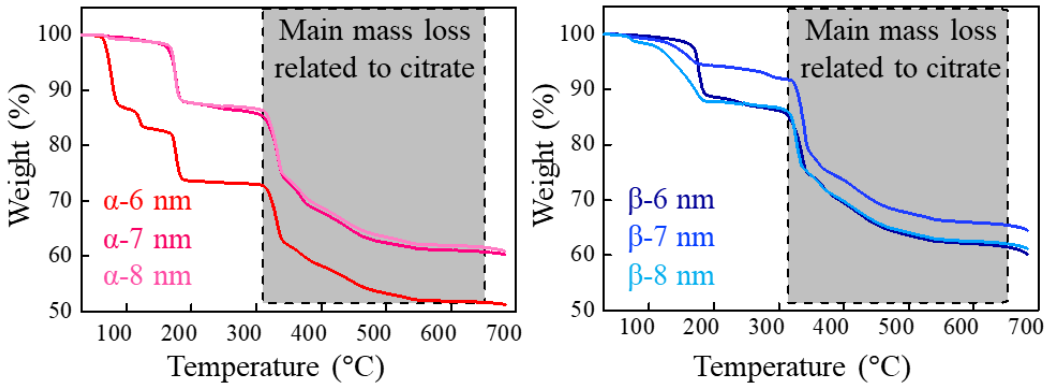

Figure 4.12. TGA profiles of cubic (α) and hexagonal (β) $NaGdF_4$ NPs collected in air atmosphere. [N. Liu et al. Nanoscale, 2019, 11, 6794.] - Reproduced by permission of The Royal Society of Chemistry.

As shown in Table 4.4, since the number of cubic NPs is larger than that of hexagonal ones in the measured samples, the estimated citrate mass on the surface of one cubic NP is less than on their counterparts. It has been reported that there are two types of interaction of $-COO^-$ groups of a citrate molecule with a particle's surface: one is called "standing up" and the particle surface interacts through only one $-COO^-$ group per citrate molecule; the other one is named "lying down" and two $-COO^-$ groups interact with the particle surface (Figure 4.13).[112, 114, 115] At low citrate coverage, the "lying down" conformation should prevail, while "lying down" and "standing up" conformations should coexist in case of high citrate coverage.[106, 111] In our study, the lower amount of citrate in cubic NPs may result in a cubic NP surface that is more easily accessed by water molecules, increasing the hydrophilicity of the NPs and to consequently bring larger d_H values (Figure 4.14). Overall, these considerations underline that cubic $NaGdF_4$ NPs of comparable TEM size exhibit higher r_1 values than hexagonal NPs

owing to their larger IS contribution originating from larger μ_{eff} (M_z) and τ_R (d_H) values, respectively.

Table 4.4. Estimated citrate mass on the surface of one $NaGdF_4$ nanoparticle (m_{cit}/NP).

	formulas	**cubic $NaGdF_4$**			**hexagonal $NaGdF_4$**		
NP diameter, d (nm)		6.1	6.9	8.2	6.3	7.1	8.2
Volumetric mass density, ρ (gcm^{-3})		5.06	5.06	5.06	5.61	5.61	5.61
Mass of one $NaGdF_4$ NP, m_{NP} ($\times 10^{-16}$ mg)	$m_{NP} = \rho \times V_{NP}$	6.02	8.71	14.62	7.34	10.51	16.20
Overall mass of citrate, m_{cit} (mg), based on TGA		1.76	1.92	1.23	1.50	2.12	1.13
Overall mass of NPs, m_{NPs} (mg), based on TGA		4.19	4.63	3.03	3.68	5.04	2.79
Number of NPs, N_{NPs} ($\times 10^{16}$)	$N_{NPs} = \frac{m_{NPs}}{m_{NP}}$	0.70	0.53	0.21	0.50	0.48	0.17
Citrate mass on the surface of one NP, m_{cit}/NP ($\times 10^{-16}$ mg)	$m_{cit}/NP = \frac{m_{cit}}{N_{NPs}}$	2.53	3.61	5.92	3.00	4.43	6.56

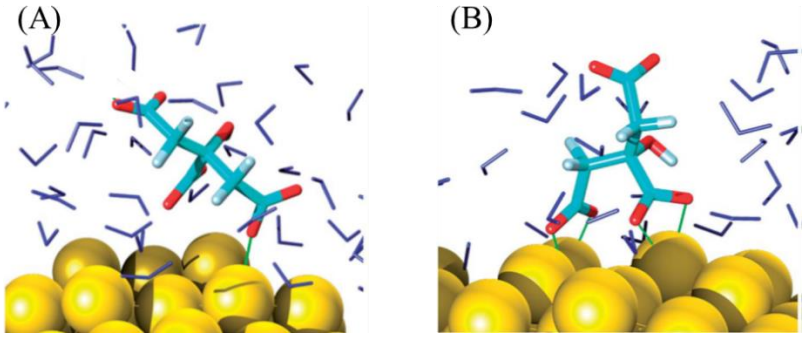

Figure 4.13. Schematic representation of the interaction between citrate molecules and the surface of a gold particle through (A) one −COO- group ("standing up" type) and (B) two −COO- groups ("lying down" type). Some of the water molecules surrounding the adsorbate are displayed as blue slim sticks. The green lines indicate distances lower then 2.6 Å. Reproduced with permission from reference 112, published by The Royal Society of Chemistry (RSC) on behalf of the Centre National de la Recherche Scientifique (CNRS) and the RSC.

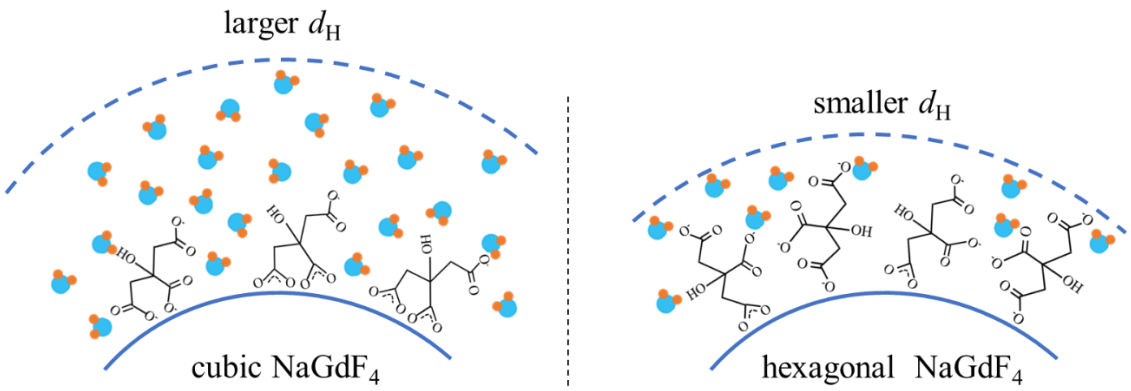

Figure 4.14. Schematic representation of the interaction between citrate molecules and the surface of $NaGdF_4$ NPs in cubic and hexagonal phases, respectively. For cubic NPs, more water molecules access to the surface of NP resulting in larger hydrodynamic diameter (d_H); for hexagonal NP, fewer accessible water molecules result in a smaller d_H.

Finally, the OS contribution stems mainly from the relaxation of water molecules that are hydrogen-bonded to the ligands and their exchange with bulk water.[57] In line with this, the increased hydrophilicity of cubic NPs, arising from a lower m_{cit} per NP, can support such bulk water exchange. However, it has elsewhere been demonstrated that, for ultrasmall $NaGdF_4$ NPs, as those reported herein, the OS contribution is less significant than the IS contribution.[57] Thus, the observed polymorph-dependent OS contribution to r_1 likely has a less prominent influence than the polymorph-dependent IS contribution.

Consequently, evaluating a set of materials and surface parameters potentially affecting r_1 in citrate-coated cubic and hexagonal NPs (Figure 4.15), superior T_1 shortening was ascribed to stronger IS contributions in NPs crystallized in the cubic lattice when compared to their hexagonal counterparts. Herein, similar total numbers of Gd^{3+} surface ions accessible for proton interaction and thus image contrast generation were determined for both polymorphs, despite the higher ρ of hexagonal $NaGdF_4$. Moreover, it was demonstrated that the phase-dependent amount of citrate per NP affected the hydrodynamic diameter d_H, being larger in

case of cubic NPs as confirmed by DLS measurements. Consequently, the interaction between Gd^{3+} surface ions and water protons was enhanced in the case of cubic NPs fostering higher r_1 values. Finally, higher r_1 for cubic $NaGdF_4$ NPs were also in agreement with polymorph-dependent trends regarding the intrinsic magnetization (M_z) reported in the literature.[109]

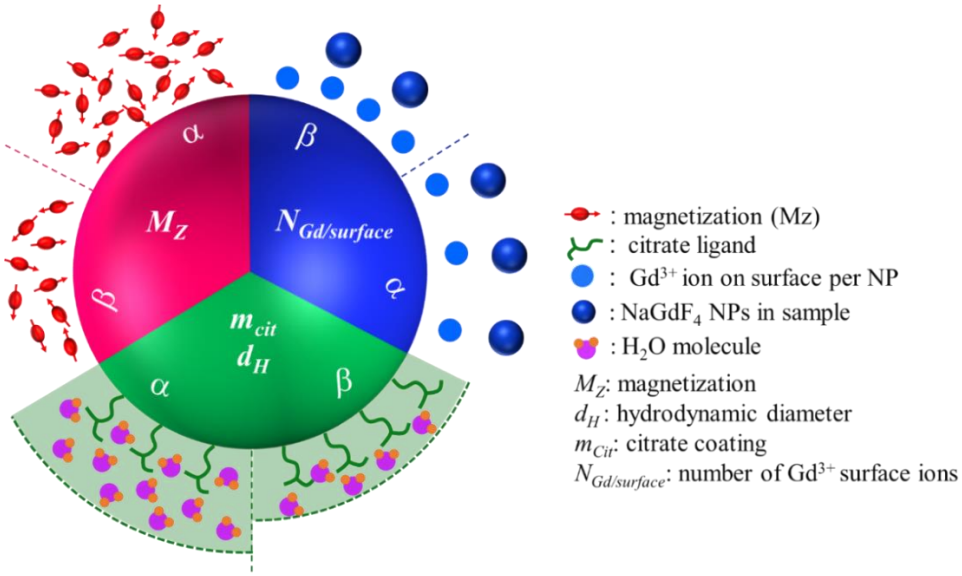

Figure 4.15. Summary of materials and surface parameters assessed to evaluate their effect on the T_1 relaxivity of citrate-coated cubic and hexagonal $NaGdF_4$ NPs. [N. Liu et al. Nanoscale, 2019, 11, 6794.] - Reproduced by permission of The Royal Society of Chemistry.

4.2.4 PAA-Coated $NaGdF_4$ Nanoparticles

In order to evaluate whether above discussed observations hold true for surface groups different from citrate, additional relaxivity studies were performed on selected NPs coated with poly(acrylic acid), PAA (8 nm-sized NPs, crystallized in the cubic as well as the hexagonal phase). PAA was chosen as an alternative ligand based on its polymeric character in contrast to the smaller citrate groups, its reported biocompatibility, and strong binding to NPs leading to colloidal stability required for MRI studies.[116] Crystallinity and size of oleate-coated NPs (pre-PAA modification) were confirmed by XRD and TEM analysis. As shown

in Figure 4.16, the XRD patterns indicated that these NPs were phase pure, while morphology and size analysis from TEM images (Figure 4.17) revealed that the NPs were monodisperse with the same size.

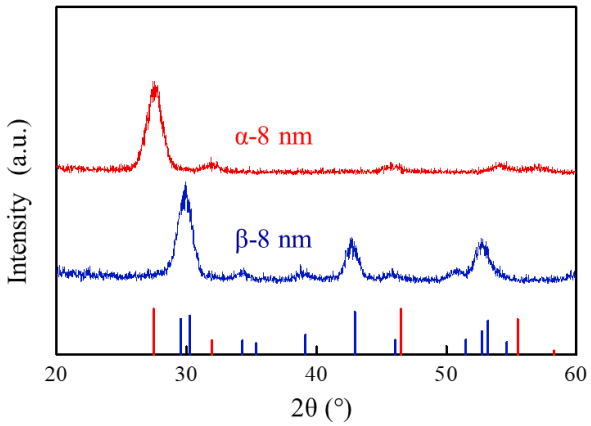

Figure 4.16. XRD patterns of cubic and hexagonal oleate-capped $NaGdF_4$ NPs with 8 nm size used for surface modification with PAA. References: red line – cubic $NaGdF_4$ (PDF card no. 00-027-0697), blue line – hexagonal $NaGdF_4$ (PDF card no. 01-080-8787). [N. Liu et al. Nanoscale, 2019, 11, 6794.] - Reproduced by permission of The Royal Society of Chemistry.

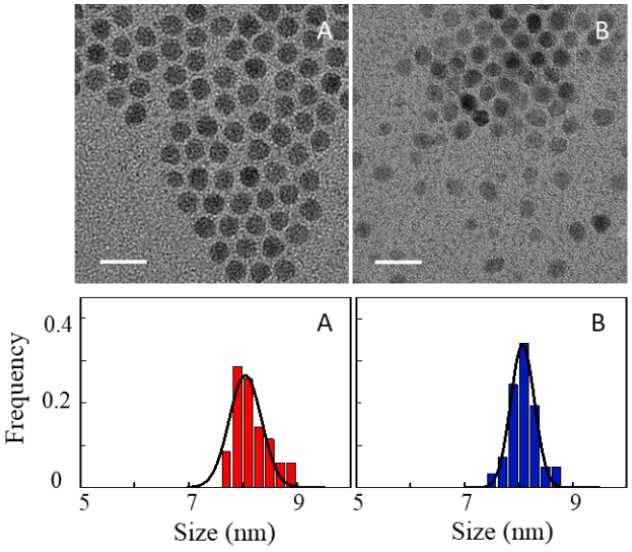

Figure 4.17. TEM images (top, scale bars are 20 nm) and size distribution histograms (bottom) of oleate-coated cubic (A) and hexagonal (B) $NaGdF_4$ NPs used for surface modification with PAA. Particle sizes of 8.11 ± 0.31 nm and 8.12 ± 0.22 nm were determined for the cubic and the hexagonal phase, respectively. Black solid lines are Gaussian fitting curves of the size distributions. [N. Liu et al. Nanoscale, 2019, 11, 6794.] - Reproduced by permission of The Royal Society of Chemistry.

PAA coating was confirmed by FTIR spectroscopy. As is shown in Figure 4.18, the FTIR spectra of both cubic and hexagonal $NaGdF_4$ NPs exhibited broad peaks at 2932 cm^{-1}, indicating the existence of C-H stretching mode of CH_2 groups.[117] Also, an intense peak was observed at 1694 cm^{-1} which was assigned as C=O stretching vibrations.[86, 117] This indicated successful coating of the samples with PAA. TEM images of PAA-coated $NaGdF_4$ NPs (Figure 4.19) confirmed that these particles were well-dispersed after coating with PAA.

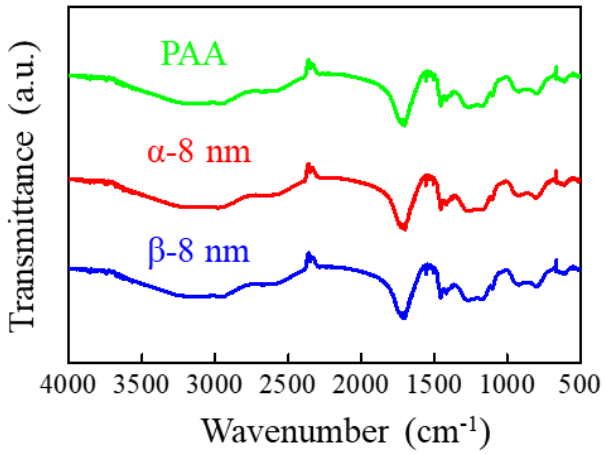

Figure 4.18. FTIR spectra of PAA-coated cubic (α) and hexagonal (β) $NaGdF_4$ NPs (TEM size: 8 nm) as well as poly(acrylic acid) (PAA) used as reference.

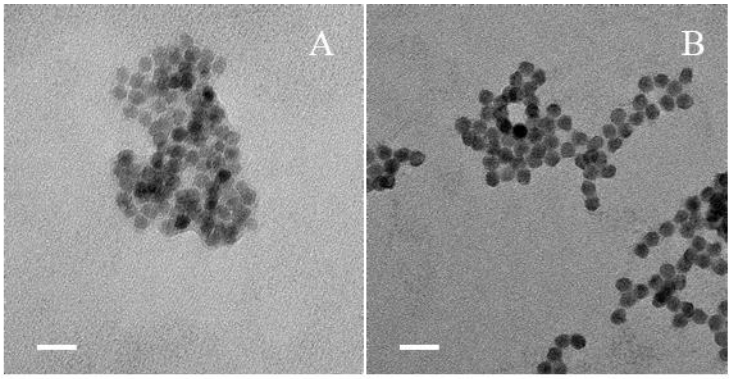

Figure 4.19. TEM images of PAA-coated $NaGdF_4$ NPs crystallized in the (A) cubic and (B) hexagonal polymorph (TEM size: 8 nm). Scale bars are 20 nm. [N. Liu et al. Nanoscale, 2019, 11, 6794.] - Reproduced by permission of The Royal Society of Chemistry.

4.2.5 MRI Relaxivity Studies of PAA-Coated $NaGdF_4$ Nanoparticles

Relaxation rates R_1 and R_2 of water protons plotted against the molar concentration of Gd^{3+} for cubic (α) and hexagonal (β) $NaGdF_4$ NPs coated with PAA are shown in Figure 4.20. In agreement with the data obtained for citrate-coated NPs, r_1 values were found to be larger in the case of the cubic polymorph, namely 4.13 mM^{-1} s^{-1} as compared to 2.78 mM^{-1} s^{-1} for the hexagonal NPs. This translates into an approximately 1.5 times larger r_1 value for the cubic NPs (compared to a factor of approximately 2 in the case of citrate-coated NPs).

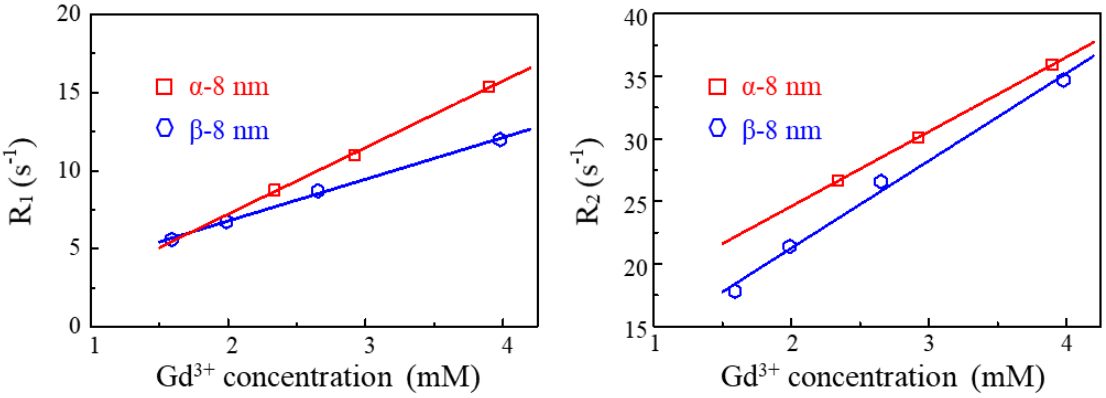

Figure 4.20. Relaxation rates R_1 (left) and R_2 (right) (= $1/T_1$ and $1/T_2$) of water protons plotted against the molar concentration of Gd^{3+} for PAA coated cubic (α) and hexagonal (β) $NaGdF_4$ NPs (TEM size: 8 nm) at 3 T. Solid lines are linear fits. Red data points and fits stand for cubic NPs, while blue data points and fits stand for hexagonal NPs. [N. Liu et al. Nanoscale, 2019, 11, 6794.] - Reproduced by permission of The Royal Society of Chemistry.

The overall lower r_1 values for PAA-coated NPs in comparison to their citrate-coated analogues may be due to the longer chain length of PAA (as opposed to the small citrate molecule) forming a brush border on the nanoparticle surface. As is shown in Figure 4.21, smaller ligand (citrate groups) will allow more water molecules to access the surface of $NaGdF_4$ NPs than the larger ligand (PAA) can do.[58] This different surface configuration of ligand relative to citrate could alter non-covalent interactions with the solvent to change r_1. A similar effect of decreasing r_1 values with increasing ligand-size has been reported for, *e.g.*,

ultrasmall Gd_2O_3 NPs.[58] Meanwhile, the r_2/r_1 ratio of cubic NPs (1.57) was smaller than that of the hexagonal counterpart (2.51). These results further corroborate the observation that cubic $NaGdF_4$ NPs produce higher image contrast as MRI T_1 shortening agents than was observed for hexagonal $NaGdF_4$ NPs.

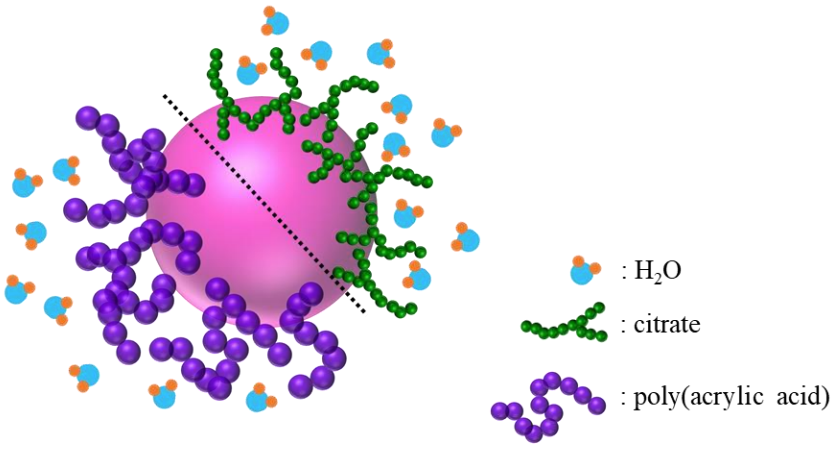

Figure 4.21. Scheme of the different surface modifications of $NaGdF_4$ NP with small molecules (citrate) and long-chain polymer (poly(acrylic acid) respectively. Small citrate molecules allow more water molecules to access to the NP surface than larger poly(acrylic acid) molecules.

DLS measurements on PAA-coated NPs revealed hydrodynamic diameters d_H of 28.0 nm for the cubic and 27.1 nm for the hexagonal polymorph (Figure 4.22). Thus, while the interaction of citrate groups with the NP surface was strongly influenced by the crystalline phase of the NPs, as reflected by their respective d_H values, no such polymorph-induced variation of the surface modification was observed in the case of PAA. Yet, notably, the r_1 value of cubic NPs was still larger than that of the hexagonal analogues. Since the difference in d_H was negligible between the samples, the observed difference in r_1 between phases can be ascribed to the difference in μ_{eff}, where cubic NPs were reported to have larger M_z (thus, μ_{eff}) values and thus, a resultant larger r_1.

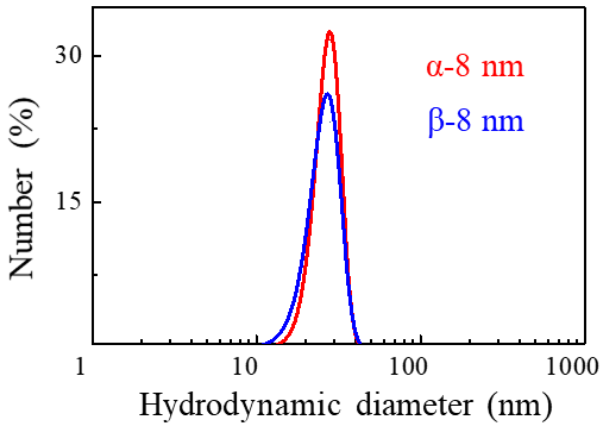

Figure 4.22. DLS curves of PAA-coated cubic (α) and hexagonal (β) $NaGdF_4$ NPs dispersed in water. [N. Liu et al. Nanoscale, 2019, 11, 6794.] - Reproduced by permission of The Royal Society of Chemistry.

4.3 Summary

A microwave-assisted approach was developed to prepare monodisperse, $NaGdF_4$ NPs crystallized in the cubic and hexagonal polymorphs covering the exact same size range. Specifically, by tuning the reaction volume and the relative amount of Na^+ and Gd^{3+} ions in the reaction mixture, size and crystalline phase were independently controlled. This provided a set of samples suitable to address effects of the NPs' crystalline phase on their performance as MRI contrast agents. MRI T_1 relaxivity measurements performed on citrate-coated samples ranging from 6 to 8 nm revealed highest r_1 values being 6 times larger than the r_1 value of clinical standard Gd-DOTA. Most importantly, it was demonstrated that r_1 values of cubic-phase citrate-coated $NaGdF_4$ NPs were approximately twice as high as those found for their hexagonal analogues. Upon thorough physicochemical characterization of the NPs, the larger r_1 featured by citrate-coated cubic $NaGdF_4$ NPs was ascribed to the reduced amount of citrate groups as a function of the crystalline phase and therewith correlated larger hydrodynamic diameter. The elevated r_1 values observed for cubic NPs were further in good agreement with

higher magnetization values previously reported in the literature. Similarly, r_1 values were found to be 1.5 times higher in case of PAA-coated cubic NPs opposed to their hexagonal analogues. Overall, this study shows that the crystalline phase of $NaGdF_4$ NPs has an effect on r_1, irrespective of the chosen surface modification. These findings are of particular interest with respect to the development of brighter MRI contrast agents for future *in vivo* biomedical applications.

Chapter 5. Alternative Lanthanide-Based Nanoparticles for MRI Applications

5.1 Introduction

Besides Gd^{3+}-based $NaLnF_4$ NPs used for MRI contrast agents, other $NaLnF_4$ NPs (Ln=Dy, Eu) are also developed for MRI applications. For instance, $NaDyF_4$ NPs, promising candidates for T_2 contrast agents at high field MRI, have been widely investigated in recent years.[10, 50] The effects of size and surface modification of $NaDyF_4$ NPs on T_2 relaxivity have been reported.[10] However, there has been no report on how T_2 relaxivity is affected by the crystalline phase of these particles. Hence, it is valuable to investigate the crystallinity-dependent relaxivity behaviour of $NaDyF_4$ NPs by preparing these particles with the same size and shape. In the meanwhile, it has been shown that ultrasmall inorganic NPs (with sizes below 6 nm) are suitable as MRI contrast agents, because they can be rapidly cleared through a renal route from the body after completing their intended roles.[118] However, the preparation of sub-6 nm NPs with lanthanide trifluoacetate (Ln-TFA) precursor is still a challenge. This is because TFA requires the cleavage of its covalent bond to producing F^- source, but this process may be not efficient which limits the nucleation and results in fewer and larger NPs.[100, 119, 120] It has been reported that Ln-oleate precursors in combination with NH_4F as a more efficient F^- source are suitable to produce ultrasmall NPs.[100, 121] Hence, Dy-oleate was selected as precursor to prepare ultrasmall $NaDyF_4$ NPs to assess their T_2 relaxivity behaviour.

In a slightly different realm, owing to the paramagnetic property of the Eu^{3+} ion, Eu^{3+}-chelates have been developed as paramagnetic CEST contrast agents.[10-12] Eu^{3+}-chelates possess relatively large frequency offsets which can enhance the CEST signals.[13,14] Hence, increasing

research efforts have been undertaken in order to describe and advance the performance of Eu^{3+}-chelates as CEST contrast agents.[10-17] Furthermore, combining Eu^{3+}-chelates with nanocarriers (*e.g.* liposomes, micelles, and proteins) have also been developed to improve the sensitivity of CEST contrast agents. However, to the best of our knowledge, there is no report on Eu^{3+}-based NPs as CEST contrast agents. NP-based MRI contrast agents, for instance, Gd^{3+}-based NPs as T_1-weighted contrast agents, have been reported to have better contrast behaviour than chelate-based contrast agents, therefore, it is valuable to develop the more potential efficient Eu^{3+}-based NPs as CEST contrast agents.

5.2 Results and Discussion

5.2.1 Synthesis of $NaDyF_4$ Nanoparticles

$NaDyF_4$ NPs in both cubic and hexagonal polymorphs were obtained *via* a modified thermal decomposition.[94] The different phases of $NaDyF_4$ NPs were controlled by adjusting the molar ratio of Na^+ to Dy^{3+} ions. The crystalline phases of $NaDyF_4$ NPs were identified by XRD (Figure 5.1).

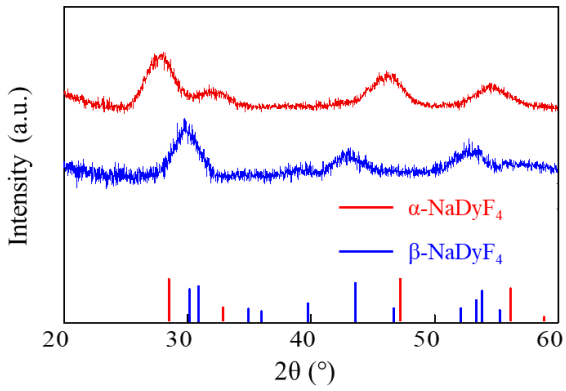

Figure 5.1. XRD patterns of cubic and hexagonal oleate-capped $NaDyF_4$ NPs. References: red line – cubic $NaDyF_4$ (PDF card no. 00-027-0697), blue line – hexagonal $NaDyF_4$ (PDF card no. 01-080-8787).

XRD patterns shown in Figure 5.1 confirmed that both phase-pure cubic and hexagonal $NaDyF_4$ NPs could be obtained (PDF card no. 00-027-0697 and PDF card no. 01-080-8787). Morphology and particle size distributions of the $NaDyF_4$ NPs are shown in Figure 5.2. Accordingly, the $NaDyF_4$ NPs were well monodisperse with uniform quasi-spherical shapes, very similar sizes of around 3 nm, and narrow size distributions.

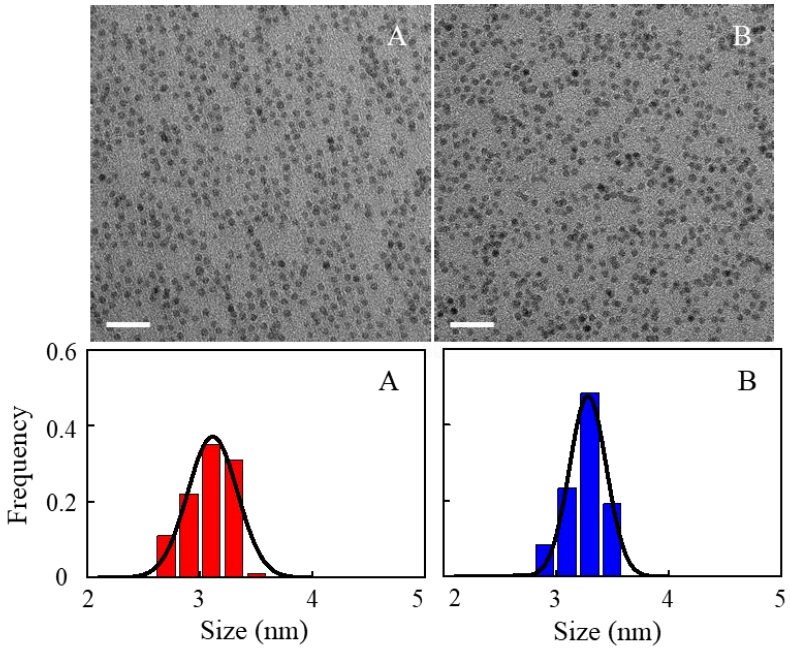

Figure 5.2. TEM micrographs (top, scale bars are 20 nm) and size distribution histograms (bottom) of oleate-capped $NaDyF_4$ NPs crystallized in the cubic α- (A) and hexagonal β-phase (B) with sizes of (A) 3.11 ± 0.22 nm and (B) 3.28 ± 0.16 nm. Black solid lines are Gaussian fitting curves of the size distributions.

The ultrasmall $NaDyF_4$ NPs (3 nm) obtained from Ln-oleate precursor indicated that the different precursors, comparing Ln-oleate and Ln-TFA precursors, indeed had an effect on particle size.[119, 120] In addition, the time-dependent pressure profiles during the synthesis with different precursors were found different (Figure 5.3). As the microwave-assisted synthesis of NPs took place in a closed system, increase in temperature, decomposition of precursors and formation of gaseous by-products resulted in pressure increase in the microwave reaction

vessels. As shown in Figure 5.3, in case of Gd-TFA precursor (red curve), the maximum pressure of 4.8 bar resulted in NPs of ca. 7 nm in size, while for Dy-oleate precursor, the pressure did not exceed 1.0 bar resulted in 3 nm sized $NaDyF_4$ NPs. The temperature-induced increase in pressure may reflect a growing precursor decomposition rate, namely higher pressure resulting larger NPs.[122, 123]

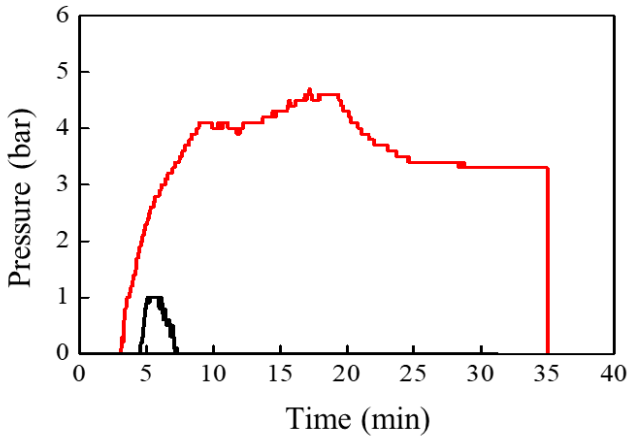

Figure 5. 3. Profiles showing the time-dependent pressure evolution during the microwave-assisted synthesis of $NaGdF_4$ NPs (7 nm) using Gd-TFA precursor (red line) and $NaDyF_4$ NPs (3 nm) using Dy-oleate precursor (black line).

5.2.2 MRI Relaxivity Studies of Citrate-Coated $NaDyF_4$ Nanoparticles

To assess the crystalline phase-dependent contrast agent behaviour of $NaDyF_4$ NPs, MRI T_1 and T_2 relaxivities of citrate-coated $NaDyF_4$ NPs in their cubic and hexagonal phases (sizes ~ 3 nm) were measured at 3 T. Relaxation rates R_1 and R_2 of water protons plotted against the molar concentration of Dy^{3+} for citrate-coated $NaDyF_4$ NPs in both phases are shown in Figure 5.4. It was found that the r_1 values of cubic and hexagonal $NaDyF_4$ NPs were very similar and small (0.04 mM^{-1} s^{-1}). This value is almost negligible because of the short electronic relaxation time of Dy^{3+} ions.[50] Notably, the r_2 value of cubic $NaDyF_4$ NPs was found larger than that of their hexagonal analogues, comparing 3.90 mM^{-1} s^{-1} to 3.11 mM^{-1} s^{-1}. These

findings confirmed once more the superior performance of the cubic phase of $NaLnF_4$ NPs: As in case of $NaGdF_4$, cubic $NaDyF_4$ NPs had a better contrast performance than their hexagonal analogues, yet, this time as MRI T_2 contrast agents. In comparison with other Dy-based nanomaterials, the r_2 value of cubic $NaDyF_4$ NPs was further found to be larger than that of 3 nm Dy_2O_3 NPs (2.17 mM^{-1} s^{-1}).[18]

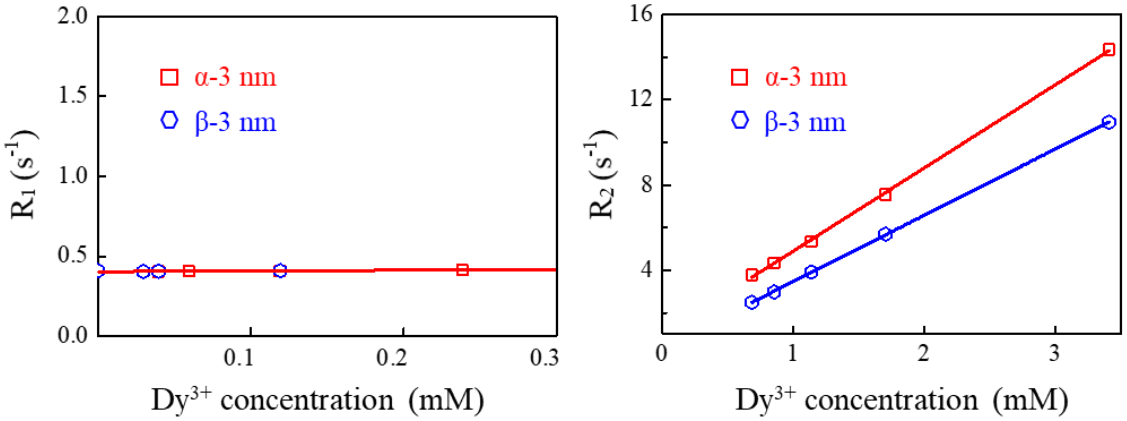

Figure 5.4. Relaxation rates R_1 (left) and R_2 (right) (= $1/T_1$ and $1/T_2$) of water protons plotted against the molar concentration of Dy^{3+} for citrate-coated cubic (α) and hexagonal (β) $NaDyF_4$ NPs (TEM size: 3 nm) at 3 T. Solid lines are linear fits. Red data points and fits stand for cubic NPs, while blue data points and fits stand for hexagonal NPs.

Further, in order to verify whether the magnetic field affects the crystallinity-dependent relaxivity behaviour, time-domain NMR relaxometry was explored to measure the T_2 relaxation times of $NaDyF_4$ NPs in both phases at 0.5 T. The corresponding T_2 relaxation rates (R_2) were plotted against the Dy^{3+} molar concentration as shown in Figure 5.5. In line with our previous observations, the obtained r_2 value for cubic NPs (2.18 mM^{-1} s^{-1}) was larger than the value found for hexagonal NPs (1.64 mM^{-1} s^{-1}). The bigger r_2 value of cubic NPs revealed that there were more water molecules interacting with the surface of cubic $NaDyF_4$ NPs, which also confirmed the superiority of cubic phase.[19]

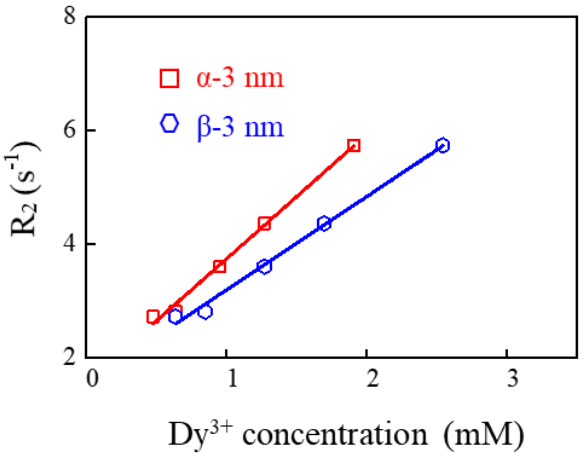

Figure 5.5. Relaxation rates R_2 (= $1/T_2$) of water protons plotted against the molar concentration of Dy^{3+} for citrate coated cubic (α) and hexagonal (β) $NaDyF_4$ NPs (TEM size: 3 nm) at 0.5 T. Solid lines are linear fits. Red data points and fit stand for cubic NPs, while blue data points and fit stand for hexagonal NPs.

5.2.3 Synthesis of $NaEuF_4$ Nanoparticles

$NaEuF_4$ NPs were synthesized by the same microwave-assisted approach used for preparing $NaGdF_4$ NPs. Crystallinity of oleate-coated $NaEuF_4$ NPs was confirmed by XRD. As shown in Figure 5.6, the XRD pattern for these NPs is in a good agreement with the cubic $NaEuF_4$ reference, indicating phase-purity for these NPs. The cubic phase was expected since a 1:1 molar ratio of Na^+ to Eu^{3+} was used. Morphology and size of the $NaEuF_4$ NPs were observed by TEM. As shown in Figure 5.7, these NPs were well monodisperse with uniform shape, and the particle size was around 7 nm. Having suitable $NaEuF_4$ NPs on hand, their surface modification with molecular CEST ligands and magnetic studies will be performed in future.

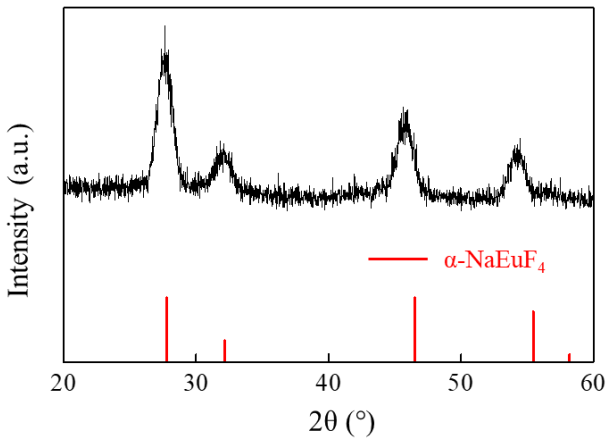

Figure 5.6. XRD pattern of cubic oleate-capped $NaEuF_4$ NPs. Reference: red line – cubic $NaEuF_4$ (PDF card no. 00-027-0697).

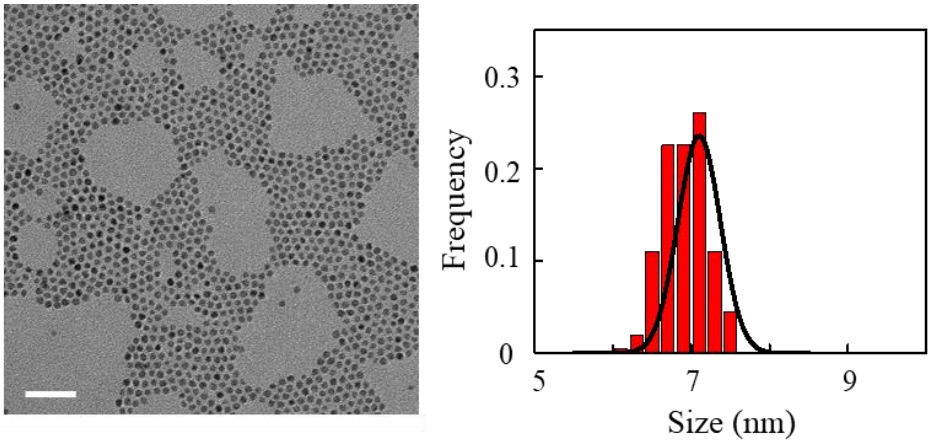

Figure 5.7. TEM micrograph (scale bar: 50 nm) and size distribution histogram of oleate-coated cubic $NaEuF_4$ NPs (size: 7.10 ± 0.27 nm).

5.2.4 Optical Property of $NaEuF_4$ Nanoparticles

Besides the magnetic property, $NaEuF_4$ NPs also exhibit an intense red photoluminescence upon irradiation with UV radiation (the energy level diagram of Eu^{3+} ions is shown in Figure 5.8).[13, 124, 125]

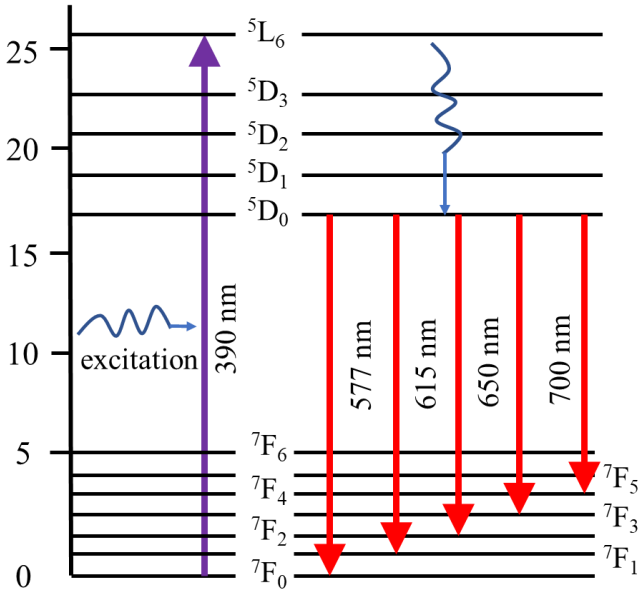

Figure 5.8. Energy level diagram for excitation and emission transitions of Eu^{3+} ions by 390 nm excitation. Redrawn from reference 121.

The photoluminescence emission spectrum of $NaEuF_4$ NPs under 390 nm excitation is shown in Figure 5.9. The expected emission peaks were observed in the red spectral region at 577, 590, 615, 650, and 700 nm stemming from the characteristic Eu^{3+} f–f transitions $^5D_0 \rightarrow {}^7F_J$, with J = 0, 1, 2, 3, 4, respectively.[20] In addition, it is known that the luminescence intensity ratio of $^5D_0 \rightarrow {}^7F_2$ (electric dipole) and $^5D_0 \rightarrow {}^7F_1$ (magnetic dipole) transition is determined by the symmetry of the crystal site in which the Eu^{3+} ions are located.[13, 126] When Eu^{3+} ions are located in a site with inversion symmetry, the emission is dominated by $^5D_0 \rightarrow {}^7F_1$ transition, while in a site without inversion symmetry, the $^5D_0 \rightarrow {}^7F_2$ transition is dominated.[13] Hence, for cubic $NaEuF_4$ NPs, it is expected that $^5D_0 \rightarrow {}^7F_1$ transition is dominated. However, as shown in Figure 5.8, we found a opposite trend, namely the $^5D_0 \rightarrow {}^7F_2$ transition is dominated (the peak corresponding to $^5D_0 \rightarrow {}^7F_2$ transition is stronger than the peak corresponding to $^5D_0 \rightarrow {}^7F_1$ transition). This result indicates the low symmetry of the coordination environment for Eu^{3+} ions in cubic $NaEuF_4$ NPs.[127] This may be because the

concentration of Eu^{3+} ions is very high in $NaEuF_4$ NPs, therefore, the distance between two neighboring Eu^{3+} ions is small enough to occur a cross-relaxation process (also known as self-quenching effect).[125, 128, 129] This cross-relaxation process may relatively quench the specific transitions, resulting a different intensity ratio between $^5D_0 \rightarrow {}^7F_2$ and $^5D_0 \rightarrow {}^7F_1$ transitions for cubic $NaEuF_4$ NPs.

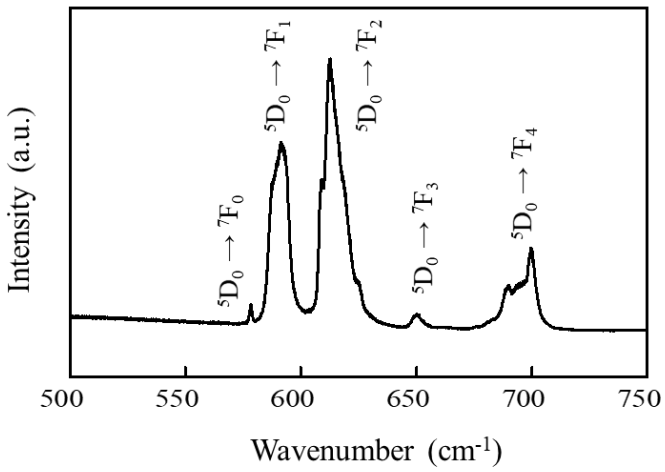

Figure 5.9. Solid state emission spectrum of $NaEuF_4$ NPs under 390 nm excitation.

5.3 Summary

To investigate the crystallinity-dependent relaxivity behaviour of $NaDyF_4$ NPs, ultrasmall cubic and hexagonal NPs (3 nm) were prepared successfully, with uniform quasi-spherical shapes and narrow size distributions. T_2 relaxivity measurements were performed on citrate-coated $NaDyF_4$ NPs in both phases at 3.0 T and 0.5 T. The results revealed that cubic $NaDyF_4$ NPs exhibited larger r_2 values than their hexagonal analogues at different magnetic fields, which indicated that cubic NPs had a better contrast performance as T_2 contrast agents. This confirmed that the crystalline phase of $NaDyF_4$ NPs had an effect on MRI T_2 relaxivity, Alternatively, cubic 7 nm sized $NaEuF_4$ NPs were synthesized as potential candidate for the

preparation of nanoparticle-supported CEST contrast agents. These $NaEuF_4$ NPs can be excited with UV light and exhibit red emission.

Chapter 6. Stability Studies with Respect to Future *in vivo* Experiments

6.1 Introduction

NPs can be engineered with precise sizes, shapes and surface chemistries as multifunctional diagnostic and therapeutic agents in medicine.[43, 130, 131] However, the effective application of NPs is often hampered by limited understanding and control over their interactions with complex biological systems, known as nano-bio interactions.[132] When NPs enter a biological environment, they rapidly adsorb proteins, forming what is known as the protein 'corona'.[133, 134] Protein corona formation is energetically favourable and features proteins in low energy state conformations with stable protein–particle interactions.[135-137] This structure can increase the hydrodynamic diameter of NP by 3 to 35 nm and may cause unexpected changes in cellular interactions, cellular uptake, biodistribution, and immunogenicity.[138-140] Therefore, understanding the nano-bio interactions is critical for developing NPs for *in vivo* applications, such as drugs delivery and contrast agents. With respect to future applications of the studied NPs, the stability studies were investigated.

6.2 Preliminary Results and Discussion

Based on the better T_1 contrast performance of cubic $NaGdF_4$ NPs in water, these NPs were selected to investigate the stability and dispersity in different buffer solutions for further *in vivo* experiments. DLS results of cubic $NaGdF_4$ NPs (TEM size: 7 nm) dispersed in different buffer solutions are shown in Figure 6.1, and the corresponding d_H are summarized in Table 6.1. As is shown in Table 6.1, the d_H of cubic NPs in pure saline was 29.64 nm while the value increased to 41.85 nm in pure phosphate-buffered saline (PBS) (pH=7.4) solution (red curves in Figure 6.1). The resulting larger d_H value in PBS solution is in agreement with

literature reports.[141, 142] The presence of phosphate groups could bind the particles, resulting in particle agglomeration.

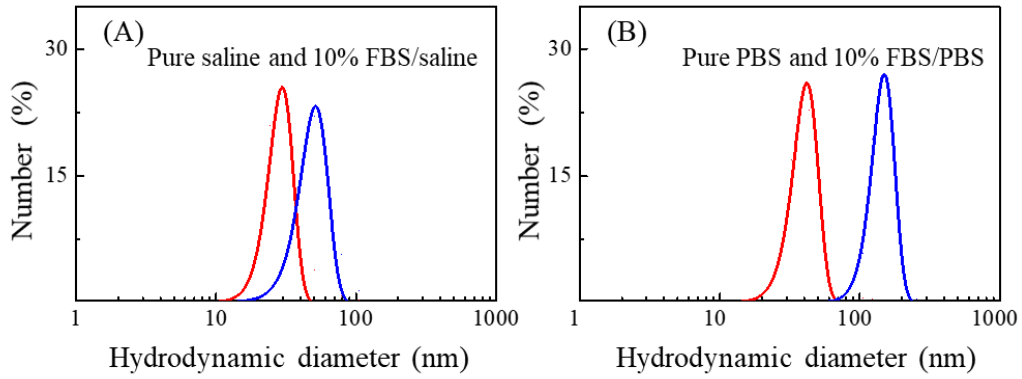

Figure 6.1. DLS curves of citrate-coated cubic $NaGdF_4$ NPs dispersed in saline solutions (red line: pure saline, blue line: 10% fetal bovine serum (FBS) saline solution), and phosphate-buffered saline (PBS) solutions (red line: pure PBS, blue line: 10% FBS/PBS solution).

Table 6.1. Hydrodynamic diameter (d_H), and polydispersity index (PDI) values obtained for cubic $NaGdF_4$ NPs in different buffer solutions.

buffer solution	**d_H (nm)**	**[PDI]**
pure saline	29.64	0.28
10% FBS/saline	51.41	0.44
pure PBS	41.85	0.32
10% FBS/PBS	149.68	0.52

When adding 10% fetal bovine serum (FBS) in saline and PBS solution, the d_H values of both solutions increased to 51.41 nm and 149.68 nm respectively. Larger d_H values are the consequence because of the presence of protein adsorption on the NP surface and cross-linking.[142-144] However, comparing with the d_H values obtained for NPs in FBS/saline

and FBS/PBS solutions, we expect that saline may be more suitable for *in vivo* experiments because of smaller d_H and PDI values.

6.3 Summary

With respect to anticipated *in vivo* bioimaging studies, the stability and dispersity of cubic $NaGdF_4$ NPs in saline and PBS solutions were investigated. The hydrodynamic diameters of NPs in pure saline and 10% FBS saline solution were smaller than that found for NPs dispersed in PBS solutions. This indicated that $NaGdF_4$ NPs possessed better dispersity in saline than in PBS solution. This showed that $NaGdF_4$-saline suspension was more suitable for investigating the nano-bio interactions for *in vivo* experiments, because there were less aggregation and interactions between NPs and saline solution.

Chapter 7. Summary and Outlook

7.1 Summary

Ln^{3+}-based NPs are promising candidates as MRI contrast agents. The work presented here aimed to investigate the effect of the crystalline phase of Ln^{3+}-based NPs on their MRI contrast performance. Understanding the phase-dependent MRI contrast behaviour of Ln^{3+}-based NPs will provide insights to the development of brighter MRI contrast agents for future *in vivo* biomedical applications.

In chapter 4, a set of $NaGdF_4$ NPs (6–8 nm) in both cubic and hexagonal polymorphs that are truly comparable in terms of size and surface chemistry were obtained by employing a microwave-assisted approach. It was found that r_1 values of cubic-phase citrate-coated $NaGdF_4$ NPs were approximately twice as high as those found for their hexagonal analogues. Key aspects were found to be a polymorph-induced larger hydrodynamic diameter and the higher magnetization possessed by cubic NPs. Similarly, r_1 values were found to be 1.5 times higher in case of PAA-coated cubic NPs opposed to their hexagonal analogues. Overall, these results show that the crystalline phase of $NaGdF_4$ NPs has an effect on r_1, irrespective of the chosen surface modification.

In chapter 5, the synthesis and characterization of 3 nm sized $NaDyF_4$ NPs was discussed in order to assess whether polymorph-dependent MRI contrast behaviour consistently exists in other Ln^{3+}-base NPs of the $NaLnF_4$ family. It was demonstrated that cubic $NaDyF_4$ NPs exhibited larger r_2 values than their hexagonal analogues at different magnetic fields (3.0 T and 0.5 T), which indicated that cubic NPs had a better contrast performance as T_2 contrast agents. This confirmed that the crystalline phase of $NaDyF_4$ NPs had an effect on MRI T_2

relaxivity. Alternatively, cubic $NaEuF_4$ NPs (7 nm) were synthesized as potential candidates for the preparation of CEST contrast agents. These $NaEuF_4$ NPs exhibited characteristic red emission upon UV light excitation.

In chapter 6, preliminary stability studies of cubic $NaGdF_4$ NPs dispersed in different buffer solutions were performed for future *in vivo* experiments. It indicated that $NaGdF_4$ NPs possessed better dispersity in saline than that in PBS solution. This showed that $NaGdF_4$-saline suspension was more suitable for investigating the nano-bio interactions for *in vivo* experiments, because there were less aggregation and interactions between NPs and saline solution.

7.2 Outlook

Our findings on the role of host crystallinity on MRI performance will help guide the development of next generation of MRI contrast agents. For instance, through tuning the crystalline lattice of the Ln^{3+}-based NPs and investigating symmetry-related changes in their M_z magnetic properties, it may obtain new materials with higher M_z values and better MRI contrast performance. $NaEuF_4$ NPs possess a larger number of Eu^{3+} ions and can also anchor plenty of molecular CEST probes (exchangeable groups) on the surface. Hence, $NaEuF_4$ NPs are proposed to be interesting candidates to be investigated as potential CEST contrast agents. Owing to the good stability and dispersity of cubic $NaGdF_4$ NPs in saline solution, these NPs are possible to be used for investigating the nano-bio interactions for future *in vivo* experiments. In addition, these NPs can also be used to study their biodistributions in the body. A good understanding of the nano-bio interactions will improve the imaging and therapeutic efficacies, and also will provide insights for nanomaterials design for their biological applications.

References

1. V. Gonzalez, D. A. Vignati, C. Leyval and L. Giamberini, *Environ. Int.*, 2014, **71**, 148.
2. M. Bethencourt, J. J. Calvino, M. Marcos and M. A. Rodrlguez-Chacon, *Corros. Sci.*, 1998, **40**, 1803.
3. M. C. Heffern, L. M. Matosziuk and T. J. Meade, *Chem. Rev.*, 2014, **114**, 4496.
4. M. Lin, Y. Zhao, S. Wang, M. Liu, Z. Duan, Y. Chen, F. Li, F. Xu and T. Lu, *Biotechnol. Adv.*, 2012, **30**, 1551.
5. S. Cotton, *Lanthanide and Actinide Chemistry*, John Wiley & Sons, Chichester, 2006.
6. E. Hemmer, F. Vetrone and K. Soga, *MRS Bulletin*, 2014, **39**, 960.
7. S. Viswanathan, K. N. Green, S. J. Ratnakar and A. D. Sherry, *Chem. Rev.*, 2010, **110**, 2960.
8. M. Norek and J. A. Peters, *Prog. Nucl. Magn. Reson. Spectrosc.*, 2011, **59**, 64.
9. R. B. Lauffer, *Chem. Rev.*, 1987, **87**, 901.
10. X. Zhang, B. Blasiak, A. J. Marenco, S. Trudel, B. Tomanek and F. C. J. M. van Veggel, *Chem. Mater.*, 2016, **28**, 3060.
11. T. C. Soesbe, S. J. Ratnakar, M. Milne, S. Zhang, Q. N. Do, Z. Kovacs and A. D. Sherry, *Magn. Reson. Med.*, 2014, **71**, 1179.
12. S. Gai, C. Li, P. Yang and J. Lin, *Chem. Rev.*, 2014, **114**, 2343.
13. K. Binnemans, *Coord. Chem. Rev.*, 2015, **295**, 1.
14. F. Auzel, *Chem. Rev.*, 2004, **104**, 139.

15. J. Zhou, Q. Liu, W. Feng, Y. Sun and F. Li, *Chem. Rev.*, 2015, **115**, 395.

16. H. B. Na and T. Hyeon, *J. Mater. Chem.*, 2009, **19**, 7.

17. C. L. Degen, H. J. Mamin, C. T. Rettner, and D. Rugar, *PNAS*, 2009, **106**, 5.

18. D. Stucht, K. A. Danishad, P. Schulze, F. Godenschweger, M. Zaitsev and O. Speck, *PLoS One*, 2015, **10**, e0133921.

19. R. Weissleder, M. Nahrendorf and M. J. Pittet, *Nat. Mater.*, 2014, **13**, 125.

20. M. Bottrill, L. Kwok and N. J. Long, *Chem. Soc. Rev.*, 2006, **35**, 557.

21. L. Zeng, D. Wu, R. Zou, T. Chen, J. Zhang and A. Wu, *Curr. Med. Chem.*, 2018, **25**, 2970.

22. H. Dong, S. R. Du, X. Y. Zheng, G. M. Lyu, L. D. Sun, L. D. Li, P. Z. Zhang, C. Zhang and C. H. Yan, *Chem. Rev.*, 2015, **115**, 10725.

23. P. Caravan, *Chem. Soc. Rev.*, 2006, **35**, 512.

24. A. S. Merbach, *The Chemistry of Contrast Agents in Medical Magnetic Resonance Imaging*, John Wiley & Sons, Ltd, Chichester, UK, 2013.

25. N. Lee and T. Hyeon, *Chem. Soc. Rev.*, 2012, **41**, 2575.

26. J. Cheon and J. Lee, *Acc. Chem. Res.*, 2008, **41**, 1630.

27. M. A. Hahn, A. K. Singh, P. Sharma, S. C. Brown and B. M. Moudgil, *Anal. Bioanal. Chem.*, 2011, **399**, 3.

28. E. L. Que and C. J. Chang, *Chem. Soc. Rev.*, 2010, **39**, 51.

29. K. N. Raymond and V. C. Pierre, *Bioconjugate Chem.*, 2005, **16**, 3.

30. G. Angelovski, *Acc. Chem. Res.*, 2017, **50**, 2215.

31. J. Wahsner, E. M. Gale, A. Rodriguez-Rodriguez and P. Caravan, *Chem. Rev.*, 2019, **119**, 957.

32. J. Lohrke, T. Frenzel, J. Endrikat, F. C. Alves, T. M. Grist, M. Law, J. M. Lee, T. Leiner, K. C. Li, K. Nikolaou, M. R. Prince, H. H. Schild, J. C. Weinreb, K. Yoshikawa and H. Pietsch, *Adv. Ther.*, 2016, **33**, 1.

33. P. H. Fries and E. Belorizky, *J. Chem. Phys.*, 2005, **123**, 124510.

34. J. C. Park, G. T. Lee, H. K. Kim, B. Sung, Y. Lee, M. Kim, Y. Chang and J. H. Seo, *ACS Appl. Mater. Interfaces*, 2018, **10**, 25080.

35. Y. I. Park, J. H. Kim, K. T. Lee, K. S. Jeon, H. B. Na, J. H. Yu, H. M. Kim, N. Lee, S. H. Choi, S. I. Baik, H. Kim, S. P. Park, B. J. Park, Y. W. Kim, S. H. Lee, S. Y. Yoon, I. C. Song, W. K. Moon, Y. D. Suh and T. Hyeon, *Adv. Mater.*, 2009, **21**, 4467.

36. M. Rogosnitzky and S. Branch, *Biometals*, 2016, **29**, 365.

37. P. Marckmann, L. Skov, K. Rossen, A. Dupont, M. B. Damholt, J. G. Heaf and H. S. Thomsen, *J. Am. Soc. Nephrol.*, 2006, **17**, 2359.

38. P. H. Kuo, E. Kanal, A. K. Abu-Alfa and S. E. Cowper, *Radiology*, 2007, **242**, 647.

39. J. G. Silvanose Biju, M. BaÇobre-Ljpez,Bella B. Manshian, Stefaan J. Soenen, and P. V. Uwe Himmelreich, *Chem. Eur. J.*, 2018, **24**, 10.

40. M. W. Ahmad, W. Xu, S. J. Kim, J. S. Baeck, Y. Chang, J. E. Bae, K. S. Chae, J. A. Park, T. J. Kim and G. H. Lee, *Sci. Rep.*, 2015, **5**, 8549.

41. N. J. J. Johnson, W. Oakden, G. J. Stanisz, R. Scott Prosser and F. C. J. M. van Veggel, *Chem. Mater.*, 2011, **23**, 3714.

42. Z. Gao, T. Ma, E. Zhao, D. Docter, W. Yang, R. H. Stauber and M. Gao, *Small*, 2016, **12**, 21.

43. C. D. Walkey, J. B. Olsen, H. Guo, A. Emili and W. C. Chan, *J. Am. Chem. Soc.*, 2012, **134**, 2139.

44. N. J. Johnson, S. He, V. A. Nguyen Huu and A. Almutairi, *ACS Nano*, 2016, **10**, 8299.

45. Z. Wei, X. Lin, M. Wu, B. Zhao, R. Lin, D. Zhang, Y. Zhang, G. Liu, X. Liu and J. Liu, *Sci. Rep.*, 2017, **7**, 5370.

46. H. Xing, S. Zhang, W. Bu, X. Zheng, L. Wang, Q. Xiao, D. Ni, J. Zhang, L. Zhou, W. Peng, K. Zhao, Y. Hua and J. Shi, *Adv. Mater.*, 2014, **26**, 3867.

47. Y. Li, T. Chen, W. Tan and D. R. Talham, *Langmuir*, 2014, **30**, 5873.

48. R. Naccache, P. Chevallier, J. Lagueux, Y. Gossuin, S. Laurent, L. Vander Elst, C. Chilian, J. A. Capobianco and M. A. Fortin, *Adv. Healthc. Mater.*, 2013, **2**, 1478.

49. R. Q. Y. Hou, F. Fang, X. Wang, C. Dong, K. Liu, C. Liu, Z. Liu, H. Lei, F. Wang and M. Gao, *ACS Nano*, 2013, **7**, 330.

50. J. Huang, Y. Hou, C. Liu, L. Jing, T. Ma, X. Sun and M. Gao, *Chem. Mater.*, 2015, **27**, 7918.

51. A. M. Schrand, M. F. Rahman, S. M. Hussain, J. J. Schlager, D. A. Smith and A. F. Syed, *Wiley Interdiscip. Rev. Nanomed. Nanobiotechnol.*, 2010, **2**, 544.

52. L. Faucher, Y. Gossuin, A. Hocq and M. A. Fortin, *Nanotechnology*, 2011, **22**, 295103.

53. A. Gee and X. Xu, *Surfaces*, 2018, **1**, 96.

54. M. Ahren, L. Selegard, A. Klasson, F. Soderlind, N. Abrikossova, C. Skoglund, T. Bengtsson, M. Engstrom, P. O. Kall and K. Uvdal, *Langmuir*, 2010, **26**, 5753.

55. F. Li, W. Gu, H. Wang, Y. Qi, Y. Deng, N. Xiao, Y. Liu, Q. Xu and L. Ye, *RSC Adv.*, 2013, **3**, 5386.

56. H. Zhang, Y. Wu, J. Wang, Z. Tang, Y. Ren, D. Ni, H. Gao, R. Song, T. Jin, Q. Li, W. Bu and Z. Yao, *Small*, 2018, **14**, 1702951.

57. A. Dash, B. Blasiak, B. Tomanek and F. C. J. M. van Veggel, *J. Phys. Chem. C*, 2018, **122**, 11557.

58. C. R. Kim, J. S. Baeck, Y. Chang, J. E. Bae, K. S. Chae and G. H. Lee, *Phys. Chem. Chem. Phys.*, 2014, **16**, 19866.

59. J. Mohapatra, A. Mitra, H. Tyagi, D. Bahadur and M. Aslam, *Nanoscale*, 2015, **7**, 9174.

60. H. Hao, Q. Ma, F. He and P. Yao, *J. Mater. Chem. B*, 2014, **2**, 7978.

61. Z. Zhao, Z. Zhou, J. Bao, Z. Wang, J. Hu, X. Chi, K. Ni, R. Wang, X. Chen, Z. Chen and J. Gao, *Nat. Commun.*, 2013, **4**, 2266.

62. G. Huang, J. Hu, H. Zhang, Z. Zhou, X. Chi and J. Gao, *Nanoscale*, 2014, **6**, 726.

63. J. T. Rosenberg, J. M. Kogot, D. D. Lovingood, G. F. Strouse and S. C. Grant, *Magn. Reson. Med.*, 2010, **64**, 871.

64. N. Blow, *Nature*, 2009, **458**, 925.

65. T. Dang, M. Suchy, Y. J. Truong, W. Oakden, W. W. Lam, C. Lazurko, G. Facey, G. J. Stanisz and A. J. Shuhendler, *Chem. Eur. J.*, 2018, **24**, 9148.

66. M. van Zijl and N. N. Yadav, *Magn. Reson. Med.*, 2011, **65**, 927.

67. S. Aime, A. Barge, D. Delli Castelli, F. Fedeli, A. Mortillaro, F. U. Nielsen and E. Terreno, *Magn. Reson. Med.*, 2002, **47**, 639.

68. G. Liu, X. Song, K. W. Chan and M. T. McMahon, *NMR Biomed.*, 2013, **26**, 810.

69. S. Zhang, K. Wu and A. D. Sherry, *J. Am. Chem. Soc.*, 2001, **123**, 1517.

70. S. Zhang, R. Trokowski and A. D. Sherry, *J. Am. Chem. Soc.*, 2003, **125**, 15288.

71. A. D. Sherry and M. Woods, *Annu. Rev. Biomed. Eng.*, 2008, **10**, 391.

72. C. X. Mao, *Wiley Interdiscip. Rev. Nanomed. Nanobiotechnol.*, 2016, **8**, 814.

73. O. M. Evbuomwan, M. E. Merritt, G. E. Kiefer and A. Dean Sherry, *Contrast. Media. Mol. Imaging*, 2012, **7**, 19.

74. P. M. Winter, K. Cai, J. Chen, C. R. Adair, G. E. Kiefer, P. S. Athey, P. J. Gaffney, C. E. Buff, J. D. Robertson, S. D. Caruthers, S. A. Wickline and G. M. Lanza, *Magn. Reson. Med.*, 2006, **56**, 1384.

75. O. Vasalatiy, R. D. Gerard, P. Zhao, X. Sun and A. D. Sherry, *Bioconjug. Chem.*, 2008, **19**, 598.

76. G. Ferrauto, F. Carniato, L. Tei, H. Hu, S. Aime and M. Botta, *Nanoscale*, 2014, **6**, 9604.

77. L. Boselli, E. Polo, V. Castagnola and K. A. Dawson, *Angew. Chem. Int. Ed.*, 2017, **56**, 4215.

78. H. Mai, R. Si, Z. Yan, L. Sun, and L. You, *J. Am. Chem. Soc.*, 2006, **128**, 11.

79. F. Vetrone, R. Naccache, V. Mahalingam, C. G. Morgan and J. A. Capobianco, *Adv. Funct. Mater.*, 2009, **19**, 2924.

80. S. Dühnen, T. Rinkel and M. Haase, *Chem. Mater.*, 2015, **27**, 4033.

81. F. Wang, Y. Han, C. S. Lim, Y. Lu, J. Wang, J. Xu, H. Chen, C. Zhang, M. Hong and X. Liu, *Nature*, 2010, **463**, 1061.

82. M. Quintanilla, F. Ren, D. Ma and F. Vetrone, *ACS Photonics*, 2014, **1**, 662.

83. H. Q. Wang, R. D. Tilley and T. Nann, *Cryst. Eng. Comm.*, 2010, **12**, 1993.

84. H. Wand and T. Nann, *ACS Nano*, 2009, **3**, 3804.

85. N. Panov, R. Marin and E. Hemmer, *Inorg. Chem.*, 2018, **57**, 14920.

86. A. Sedlmeier and H. H. Gorris, *Chem. Soc. Rev.*, 2015, **44**, 1526.

87. F. Wang, D. Banerjee, Y. Liu, X. Chen and X. Liu, *Analyst.*, 2010, **135**, 1839.

88. C. Duan, L. Liang, L. Li, R. Zhang and Z. P. Xu, *J. Mater. Chem. B*, 2018, **6**, 192.

89. H. T. T. Duong, Y. Chen, S. A. Tawfik, S. Wen, M. Parviz, O. Shimoni and D. Jin, *RSC Adv.*, 2018, **8**, 4842.

90. Y. Chen, H. T. T. Duong, S. Wen, C. Mi, Y. Zhou, O. Shimoni, S. M. Valenzuela and D. Jin, *Anal. Chem.*, 2018, **90**, 663.

91. R. Naccache, V. Mahalingam, L. A. Cuccia and J. A. Capobianco, *Chem. Mater.*, 2009, **21**, 717.

92. C. A. Traina and J. Schwartz, *Langmuir*, 2007, **23**, 9158.

93. A. Skripka, R. Marin, A. Benayas, P. Canton, E. Hemmer and F. Vetrone, *Phys. Chem. Chem. Phys.*, 2017, **19**, 11825.

94. T. Rinkel, A. N. Raj, S. Duhnen and M. Haase, *Angew. Chem. Int. Ed.*, 2016, **55**, 1164.

95. N. Bogdan, E. M. Rodriguez, F. Sanz-Rodriguez, M. C. de la Cruz, A. Juarranz, D. Jaque, J. G. Sole and J. A. Capobianco, *Nanoscale*, 2012, **4**, 3647.

96. G. Chen, T. Y. Ohulchanskyy, S. Liu, W. C. Law, F. Wu, M. T. Swihart, H. Agren and P. N. Prasad, *ACS Nano*, 2012, **6**, 2969.

97. A. Dong, X. Ye, J. Chen, Y. Kang, T. Gordon, J. M. Kikkawa and C. B. Murray, *J. Am. Chem. Soc.*, 2011, **133**, 998.

98. H. Zhang, Y. Li, I. A. Ivanov, Y. Qu, Y. Huang and X. Duan, *Angew. Chem. Int. Ed.*, 2010, **49**, 2865.

99. X. F. Qiao, J. C. Zhou, J. W. Xiao, Y. F. Wang, L. D. Sun and C. H. Yan, *Nanoscale*, 2012, **4**, 4611.

100. D. Ostrowski, D. J. Gargas, E. M. Katz, G. Han, P. J. Schuck, D. J. Milliron and B. E. Cohen, *ACS Nano*, 2012, **6**, 2686.

101. B. Voss, J. Nordmann, A. Uhl, R. Komban and M. Haase, *Nanoscale*, 2013, **5**, 806.

102. F. Carniato, K. Thangavel, L. Tei and M. Botta, *J. Mater. Chem. B*, 2013, **1**, 2442.

103. T. Vairapperumal, A. Saraswathy, J. S. Ramapurath, S. Kalarical Janardhanan and N. Balachandran Unni, *Sci. Rep.*, 2016, **6**, 34976.

104. H. B. Martin Rohrer, Jan Mintorovitch, and M. R. a. H.-J. Weinmann, *Invest. Radiol.*, 2005, **40**, 10.

105. E. Gianolio, E. D. Gregorio and S. Aime, *Eur. J. Inorg. Chem.*, 2019, **2019**, 137.

106. P. Ivanchenko, J. M. Delgado-Lopez, M. Iafisco, J. Gomez-Morales, A. Tampieri, G. Martra and Y. Sakhno, *Sci. Rep.*, 2017, **7**, 8901.

107. I. Solomon, *Phys. Rev.*, 1955, **99**, 559.

108. N. Bloembergen and L. O. Morgan, *J. Chem. Phys.*, 1961, **34**, 842.

109. E. M. Rodrigues, D. A. Gálico, M. A. Lemes, J. Bettini, E. T. Neto, I. O. Mazali, M. Murugesu and F. A. Sigoli, *New J. Chem.*, 2018, **42**, 13393.

110. M. E. McHenry and D. E. Laughlin, *Magnetic moment and magnetization*, Carnegie Mellon University, Pittsburgh, 2009.

111. Y. Y. Hu, A. Rawal and K. Schmidt-Rohr, *Proc. Natl. Acad. Sci. USA*, 2010, **107**, 22425.

112. S. Monti, G. Barcaro, L. Sementa, V. Carravetta and H. Ågren, *RSC Adv.*, 2017, **7**, 49655.

113. J. W. Park and J. S. Shumaker-Parry, *J. Am. Chem. Soc.*, 2014, **136**, 1907.

114. Z. Wang, Z. Xu, W. Zhao, W. Chen, T. Miyoshi and N. Sahai, *ACS Appl. Mater. Interfaces*, 2016, **8**, 28116.

115. H. Al-Johani, E. Abou-Hamad, A. Jedidi, C. M. Widdifield, J. Viger-Gravel, S. S. Sangaru, D. Gajan, D. H. Anjum, S. Ould-Chikh, M. N. Hedhili, A. Gurinov, M. J. Kelly, M. El Eter, L. Cavallo, L. Emsley and J. M. Basset, *Nat. Chem.*, 2017, **9**, 890.

116. S. L. Ho, H. Cha, I. T. Oh, K.-H. Jung, M. H. Kim, Y. J. Lee, X. Miao, T. Tegafaw, M. Y. Ahmad, K. S. Chae, Y. Chang and G. H. Lee, *RSC Adv.*, 2018, **8**, 12653.

117. Y. Liu, D. Tu, H. Zhu and X. Chen, *Chem. Soc. Rev.*, 2013, **42**, 6924.

118. J. Liu, G. Chen, S. Hao and C. Yang, *Nanoscale*, 2017, **9**, 91.

119. H. P. J. Ryu, K. Kim, H. Kim, J. H. Yoo, M. Kang, K. Im, R. Grailhe and R. Song, *J. Phys. Chem. C*, 2010, **114**, 21077.

120. P. Ghosh and A. Patra, *J. Phys. Chem. C*, 2008, **112**, 3223.

121. B. Amouroux, C. Roux, J. D. Marty, M. Pasturel, A. Bouchet, M. Sliwa, O. Leroux, F. Gauffre and C. Coudret, *Inorg. Chem.*, 2019, **58**, 5082.

122. N. T. K. Thanh, N. Maclean and S. Mahiddine, *Chem. Rev.*, 2014, **114**, 7610.

123. V. K. LaMer and R. H. Dinegar, *J. Am. Chem. Soc.*, 1950, **72**, 4847.

124. L. Schneider, T. Rinkel, B. Voss, A. Chrobak, J. P. Klare, J. Neethling, J. Olivier, D. Schaniel, E. Bendeif el, F. Bondino, E. Magnano, I. Pis, K. Balinski, J. Wollschlager, H. J. Steinhoff, M. Haase and K. Kuepper, *Nanoscale*, 2016, **8**, 2832.

125. J. Rajagukguk, J. Kaewkhao, M. Djamal, R. Hidayat, Suprijadi and Y. Ruangtaweep, *J. Mol. Struct.*, 2016, **1121**, 180.

126. Z. Xu, Q. Zhao, F. Ding and Y. Sun, *Mater. Res. Bull.*, 2013, **48**, 2797.

127. R. M. D. Zakaria, D. Avignant and M. Zahir, *J. Alloy. Compd.*, 1997, **257**, 65.

128. Y. Zhang and X. Liu, *Nat. Nanotechnol.*, 2013, **8**, 702.

129. L. G. Van Uitert and L. F. Johnson, *J. Chem. Phys.*, 1966, **44**, 3514.

130. C. D. Walkey and W. C. Chan, *Chem. Soc. Rev.*, 2012, **41**, 2780.

131. N. Liu, R. Marin, Y. Mazouzi, G. O. Cron, A. Shuhendler and E. Hemmer, *Nanoscale*, 2019, **11**, 6794.

132. A. Albanese, P. S. Tang and W. C. Chan, *Annu. Rev. Biomed. Eng.*, 2012, **14**, 1.

133. T. Cedervall, S. Lindman, T. Berggard, E. Thulin, H. Nilsson, K. A. Dawson and S. Linse, *PNAS*, 2007, **104**, 2050.

134. M. P. Monopoli, D. Walczyk, A. Campbell, G. Elia, I. Lynch, F. B. Bombelli and K. A. Dawson, *J. Am. Chem. Soc.*, 2011, **133**, 2525.

135. J. Lazarovits, Y. Y. Chen, E. A. Sykes and W. C. Chan, *Chem. Commun.*, 2015, **51**, 2756.

136. T. P. E. Casals, A. Duschl, G. J. Oostingh and V. Puntes, *ACS Nano*, 2010, **4**, 3623.

137. A. A. Vertegel, R. W. Siegel and J. S. Dordick, *Langmuir*, 2004, **20**, 6800.

138. M. A. Dobrovolskaia, A. K. Patri, J. Zheng, J. D. Clogston, N. Ayub, P. Aggarwal, B. W. Neun, J. B. Hall and S. E. McNeil, *Nanomedicine*, 2009, **5**, 106.

139. M. P. Monopoli, C. Aberg, A. Salvati and K. A. Dawson, *Nat. Nanotechnol.*, 2012, **7**, 779.

140. H. S. Choi, W. Liu, P. Misra, E. Tanaka, J. P. Zimmer, B. Itty Ipe, M. G. Bawendi and J. V. Frangioni, *Nat. Biotechnol.*, 2007, **25**, 1165.

141. T. M. Sager, D. W. Porter, V. A. Robinson, W. G. Lindsley, D. E. Schwegler-Berry and V. Castranova, *Nanotoxicology*, 2009, **1**, 118.

142. A. E. Nel, L. Madler, D. Velegol, T. Xia, E. M. Hoek, P. Somasundaran, F. Klaessig, V. Castranova and M. Thompson, *Nat. Mater.*, 2009, **8**, 543.

143. D. D. S. Tenzer, S. Rosfa, A. Wlodarski, J. Kuharev, A. Rekik, S. K. Knauer, C. Bantz, T. Nawroth, C. Bier, J. Sirirattanapan, W. Mann, L. Treuel, R. Zellner, M. Maskos, H. Schild and R. H. Stauber, *ACS Nano*, 2011, **5**, 7155.

144. W. H. Kapralov, A. A. Amoscato, N. Yanamala, K. Balasubramanian, D. E. Winnica, E. R. Kisin, G. P. Kotchey, P. Gou, L. J. Sparvero, P. Ray, R. K. Mallampalli, J.

Klein-Seetharaman, B. Fadeel, A. Star, A. A. Shvedova and V. E. Kagan, *ACS Nano*, 2012, **6**, 4147.